

Quantum enhanced parameter estimation with monitored quantum nonequilibrium systems using inefficient photo detection

Albert Cabot,¹ Federico Carollo,² and Igor Lesanovsky^{1,3,4}

¹*Institut für Theoretische Physik and Center for Integrated Quantum Science and Technology, Universität Tübingen, Auf der Morgenstelle 14, 72076 Tübingen, Germany.*

²*Centre for Fluid and Complex Systems, Coventry University, Coventry, CV1 2TT, United Kingdom*

³*School of Physics and Astronomy, University of Nottingham, Nottingham, NG7 2RD, UK.*

⁴*Centre for the Mathematics and Theoretical Physics of Quantum Non-Equilibrium Systems, University of Nottingham, Nottingham, NG7 2RD, UK*

Many-body quantum systems hosting emergent collective behavior bear the promise to enable quantum enhanced parameter estimation. Formally this means that the variance of the parameter to be estimated decreases faster than N^{-1} , where N is the number of particles forming the quantum system. In practice such scaling is challenging to achieve as the underlying many-body correlations are fragile. Moreover, devising the optimal measurements that indeed tap the quantum enhancement is often rather involved. Here we show that the inefficient detection of the photo emission from a dissipative quantum many-body system is sufficient to reach quantum enhanced parameter estimation even when some loss channels remain completely unmonitored. We illustrate our approach by considering the so-called boundary time-crystal, which is a nonequilibrium many-body system that has been realized recently experimentally in cold atomic gases. By analyzing the structure of the temporal correlations of its emission field, we are able to construct a family of near optimal parameter estimation measurements with a simple interferometric setup.

I. INTRODUCTION

Quantum correlations and collective phenomena in many-body systems can serve as a resource for sensing applications [1, 2]. Examples include protocols to detect small displacements or weak electromagnetic fields in systems of trapped ions [3], or Rydberg atoms [4, 5]. In these settings, the number of particles, N , represents a resource for increasing the precision of sensors and quantum effects can lead to enhanced scalings of the sensitivity with it. The variance of the estimate of a quantity of interest can indeed pass from decreasing with the scaling N^{-1} , the so-called standard quantum limit, to N^{-2} , the so-called Heisenberg limit, in the presence of quantum correlations [1, 2]. The Heisenberg scaling with the number of particles has been observed, for instance, in protocols exploiting so-called N00N entangled states to estimate small phases [6]. However, the practical implementation of these quantum enhanced protocols is typically challenging due to both the susceptibility of quantum systems to decoherence effects, suppressing quantum correlations, and to the difficulty of preparing N00N states for large systems [1]. Another route to achieve quantum-enhanced sensing is through the use of spin squeezed states, which allow one to, e.g., surpass the standard quantum limit in the estimation of phases [7–9]. Large clouds of atoms can be prepared in spin squeezed states by trapping them in high-finesse optical cavities. Here the coupling between the atoms and the cavity modes can be leveraged to generate spin squeezing [9, 10], for instance by engineering collective Hamiltonian interactions or by implementing feedback protocols based on the detection of the cavity output [11–14]. This last example shows that dissipative and noisy effects can actually play an active role in the

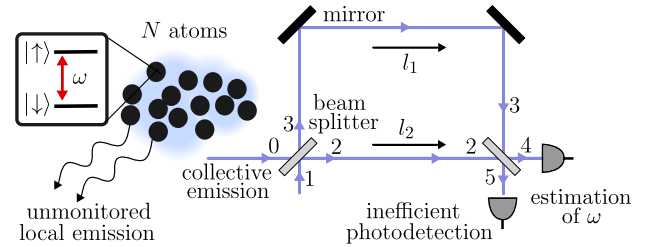


FIG. 1. **Sketch of the system and measurement protocol.** We consider an ensemble of N two-level atoms, emitting collectively and driven at resonance with Rabi frequency ω . We are interested in the estimation of small variations of ω by analyzing the light that is emitted collectively. In a realistic setting also unmonitored decay channels exist; here, due to local photon emission. The measurement protocol involves a Mach-Zehnder interferometer. The collective emission of the system is input into arm '0', while vacuum is input into arm '1'. Photodetectors, which may be inefficient, are placed at the output arms '4' and '5'. The difference in path length $l_1 - l_2$ is chosen such that we can probe the field emitted at two times of interest.

design of sensing protocols.

Sensing via continuous monitoring [15] exploits the emission signal of a dissipative quantum system to perform parameter estimation [16–26]. On the one hand, this allows one to gather the information the system emits into the environment through the different decay channels. Here, fundamental sensitivity bounds based on the Quantum Fisher Information (QFI) have been derived [27–31], and general optimal measurement strategies reported [32, 33]. On the other hand, the combination of driving, monitoring and dissipation in many-body

systems can give rise to emergent nonequilibrium phases and phase transitions [34–36]. This collective behavior can also constitute a resource for sensing: near nonequilibrium phase transitions systems can display a high susceptibility to small perturbations, which can be exploited in sensing protocols, as shown both theoretically [24, 26, 30, 37–41] and experimentally [42]. Nonequilibrium phases, such as synchronized phases of atomic dipoles, can further increase the coherence time which is a key resource for phase estimation [43–45]. Both aspects can work together in quantum optical systems, where collective many-body behavior leaves a footprint in the emitted light which can be subsequently used for sensing applications.

Paradigmatic systems in this context are cooperative resonance fluorescence models [46–48], that have recently gathered attention in the context of time crystals [49] and nonequilibrium superradiant transitions, as experimentally observed in dense pencil-shaped atomic clouds [50–52]. Time-crystal phases are characterized by spontaneous time-translation symmetry breaking in the thermodynamic limit of large particle numbers, which can occur in a variety of settings and due to very different mechanisms [49, 53–69]. Experimental observations of time crystals have been reported for driven-dissipative atomic clouds and condensates [70, 71], in which their signatures are imprinted in the emitted light. They have also been previously studied in the context of sensing [40, 72–74]. For example, in Ref. [72] we have analyzed properties of the light emitted by a time crystal and its use for parameter estimation. We found that Heisenberg scaling in particle number can be achieved for the QFI. The enhanced sensitivity can be exploited through an intricate protocol that requires a cascaded system and assumes that all emissions can be monitored [72]. This also reiterates the fact that protocols based on exploiting the full emitted light field face the general practical challenges posed by i) inefficient detection and unmonitored decay channels which are present in realistic settings as well as ii) the need of complex measurements schemes, e.g., involving cascaded systems. Therefore, a fundamental and practical question is whether quantum enhanced sensitivity can be observed in the presence of such imperfections [75–78] and by performing simple measurements of the emitted light field.

In this paper, we tackle this question by considering the limit of very inefficient photo detection, in which we only detect a small fraction of the collectively emitted photons (see Fig. 1). Within this scenario, we consider measurements which solely make use of the information in the emitted field at a single time or of two-time light-field correlations at most. The latter are implemented using an interferometer, as depicted in Fig. 1. For the sake of concreteness, we illustrate our ideas exploiting a many-body system featuring a time-crystal phase. Our main result is that the Heisenberg scaling with particle number can still be observed with inefficient two-time measurements based on photo detection of the output of

an interferometer (Secs. IV and V). Moreover, we show that such scaling is still displayed in the presence of weak local decay events and for a transient time, while we propose necessary changes in the sensing protocol in order to exploit the enhanced sensitivity in such a case (Sec. VI). The limit of very inefficient sensing discussed here can be seen as a worst case scenario and thus our results highlight that Heisenberg scaling can be robustly achieved. They further demonstrate that the quantum enhanced sensitivity witnessed by the QFI of the emitted light field can indeed be retrieved by means of simple measurement schemes. Our findings thus shed new light on properties of the collectively emitted field in many-body phases and may find application in the development of quantum enhanced sensing protocols in current quantum optics setups.

II. THE MODEL

The system we consider consists of an ensemble of N two-level atoms undergoing collective processes as described by the following Markovian master equation for the state of the system ρ ($\hbar = 1$ hereafter):

$$\partial_t \rho = \mathcal{L}\rho = -i\omega[S_x, \rho] + \Gamma \left(S_- \rho S_+ - \frac{1}{2} \{S_+ S_-, \rho\} \right). \quad (1)$$

Here, \mathcal{L} is the Liouvillian superoperator and we have defined the total angular momentum operators $S_\alpha = \frac{1}{2} \sum_{j=1}^N \sigma_\alpha^{(j)}$ ($\alpha = x, y, z$) with $\sigma_\alpha^{(j)}$ being the Pauli matrices associated with atom j and $S_\pm = S_x \pm iS_y$. An extension of Eq. (1) to include the effects of local spontaneous emissions from the atoms is introduced and analyzed in Sec. VI.

The model in Eq. (1) provides a tractable scenario where collective nonequilibrium phenomena emerge and can be resolved through the statistics of the emitted light [48] or through continuous monitoring protocols [79, 80]. Eq. (1) preserves the total angular momentum of the ensemble, which makes the eigenstates of S^2 and S_z a convenient basis for the Hilbert space. Throughout the work, we consider initial conditions in the maximum total angular momentum sector, $S = N/2$, as e.g., with all atoms in the excited or in the ground state. In these conditions and for large system sizes, the system displays a crossover between two dynamical regimes separated around $\omega_c = N\Gamma/2$ [48]. For $\omega < \omega_c$, the system displays a fast overdamped relaxation to the stationary state. For $\omega > \omega_c$, the system displays an oscillatory decay to the stationary state. The quality factor of these oscillations increases linearly with system size [48, 66]. In the thermodynamic limit, these oscillations become nondecaying resulting in the emergence of a time-crystal phase [49], which is described by the mean-field equations of motion [81]. In turn, the crossover becomes a sharp nonequilibrium phase transition. We note that in order to properly analyze the thermodynamic limit one should rescale the

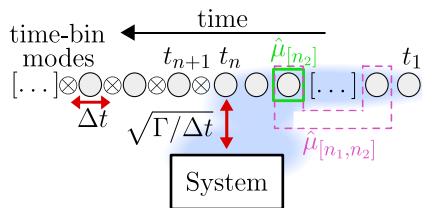


FIG. 2. **Sketch of the discrete time representation of the input-output field.** The input-output field is discretized in time bins of length Δt such that $t_n = n\Delta t$ with $n = 1, 2, \dots$. Each bin is represented by an independent bosonic mode (time-bin modes), that interacts with the system for a time window Δt and with strength $\sqrt{\Gamma/\Delta t}$. In the sketch the system has already interacted with the first n time-bin modes. Hence, the output field is formed by the time-bin modes $[1, n]$, which are generally in a nonseparable state which is also correlated with the system itself (here pictorially represented as a blue shadow). The input field is given by bins $[n+1, \infty)$, which are in a product vacuum state. The reduced state of the time-bin mode n_2 , which has already interacted with the system, is denoted by $\hat{\mu}_{[n_2]}$. The reduced state of time-bin modes n_1 and n_2 ($n_2 > n_1$), that have already interacted with the system, is denoted by $\hat{\mu}_{[n_1, n_2]}$. In this work we focus on parameter estimation based on the information contained in these reduced states of the emitted light field.

decay rate with system size, i.e. $\Gamma \rightarrow \Gamma/N$ [49, 81]. In this work we focus on finite systems for which the above rescaling is not necessary. This also allows us to directly connect with experimental systems based on atom-cavity setups [82, 83] or dense pencil-shaped atomic clouds [50].

III. DISCRETE TIME REPRESENTATION OF THE EMISSION FIELD

In this section we introduce a discrete time description of the system-emission dynamics coarse grained over the time scales in which the master equation in Eq. (1) is valid. This approach, based on the input-output formalism [84], provides a convenient way to analyze the information transferred from the system to the output field [19, 27, 32, 85, 86]. An illustration of the idea behind this formalism is presented in Fig. 2. The input-output field is discretized in time bins of length Δt , the so-called *time-bin modes*, each of them corresponding to an independent bosonic mode. When measuring all of them we recover the case of ideal continuous monitoring, while when we trace them out we recover the master equation dynamics. In this work, we are interested in the reduced states of just one and two time-bin modes $\hat{\mu}_{[n_2]}$ and $\hat{\mu}_{[n_1, n_2]}$ [cf. Fig. 2], which contain the output of the system at one or two times, respectively. These allow us, for instance, to analyze the photo detection statistics at these times, using e.g. an interferometer (see Fig. 1). The reader who is not interested in the mathematical details of this description can jump to Sec. IV, in which

we discuss the fundamental bounds to sensing using the whole emitted light or only the reduced light field states $\hat{\mu}_{[n_2]}$ and $\hat{\mu}_{[n_1, n_2]}$.

A. System and environment model

We employ the so-called quantum input-output formalism [84], in which the Hamiltonian in the laboratory frame for the system and environment is given by the sum of the following terms:

$$\begin{aligned} H_S(t) &= \omega_0 S_z + \frac{\omega}{2} (S_+ e^{-i\omega_0 t} + S_- e^{+i\omega_0 t}), \\ H_E &= \int d\nu \nu a^\dagger(\nu) a(\nu), \\ V_{SE} &= i\sqrt{\frac{\Gamma}{2\pi}} \int_{\omega_0 - \mathcal{B}}^{\omega_0 + \mathcal{B}} d\nu [S_- a^\dagger(\nu) - S_+ a(\nu)]. \end{aligned} \quad (2)$$

Here $a(\nu)$, $a^\dagger(\nu)$ are bosonic annihilation and creation operators, $[a(\nu), a^\dagger(\nu')] = \delta(\nu - \nu')$, representing the light field at frequency ν . $2\mathcal{B}$ is the bandwidth of the system environment coupling, which is small compared to ω_0 ($\omega_0 \gg \omega, \Gamma$ is also assumed) [19]. In the interaction picture with respect to $\omega_0 S_z + H_E$, we obtain the following Hamiltonian:

$$H_{SE}(t) = \omega S_x + i\sqrt{\Gamma} [S_- a^\dagger(t) - S_+ a(t)], \quad (3)$$

where

$$a(t) = \frac{1}{\sqrt{2\pi}} \int_{\omega_0 - \mathcal{B}}^{\omega_0 + \mathcal{B}} d\nu a(\nu) e^{-i(\nu - \omega_0)t}. \quad (4)$$

We consider the dynamics coarse grained on a timescale much larger than \mathcal{B}^{-1} . At this scale, the field operators $a(t)$ satisfy $[a(t), a^\dagger(t')] = \delta(t - t')$ [84]. A discrete-time dynamics can be derived by considering discrete time steps that are small compared to the relaxation timescales of Eq. (1), but much larger than the coarse graining timescale $\Delta t \gg \mathcal{B}^{-1}$ [19, 32, 85, 86]. Then the time window $[0, T)$ is split in M time bins, denoted with the label $[n] = [t_{n-1}, t_n)$, where $t_n = n\Delta t$ and $T = M\Delta t$. Following Refs. [19, 86], for each time bin we define the coarse-grained field operators:

$$b_{[n]} = \frac{1}{\sqrt{\Delta t}} \int_{t_{n-1}}^{t_n} d\tau a(\tau), \quad (5)$$

which satisfy bosonic commutation relations $[b_{[n]}, b_{[n']}^\dagger] = \delta_{nn'}$. Each of these bosonic modes defines an independent piece of the light field, or *time-bin mode*, for which there is an associated Fock space: $|\sigma_n\rangle = b_{[n]}^{\dagger\sigma} |0_n\rangle / \sqrt{\sigma!}$ with $\sigma_n = 0, 1, 2, \dots$. The time evolution can then be approximated (up to order Δt) by:

$$\begin{aligned} U_{SE}^{[n]}(\Delta t) &\approx 1 - i\omega S_x \Delta t + \sqrt{\Gamma \Delta t} (S_- b_{[n]}^\dagger - \text{H.c.}) \\ &\quad - \frac{\Gamma \Delta t}{2} (S_+ S_- b_{[n]} b_{[n]}^\dagger + \text{H.c.}) \\ &\quad + \frac{\Gamma \Delta t}{2} (S_-^2 b_{[n]}^{\dagger 2} + \text{H.c.}). \end{aligned} \quad (6)$$

Considering the initial uncorrelated system-field state $|\Psi(0)\rangle = |\psi_S(0)\rangle \otimes (\otimes_{n=1}^{\infty} |0_n\rangle)$, we recover the master equation (1) after evolving each time step with the unitary operator in Eq. (6), tracing out the time-bin modes, and performing the continuum limit or short time limit ($\Delta t \rightarrow 0$) [32, 86]. When instead explicitly considering the emission field, we can restrict the time-bin modes Hilbert space to $\sigma_n = 0, 1$ as long as Δt is small enough [19, 32, 85, 86]. This is analogous to the assumption made in photocounting unravellings in which a time step Δt is chosen small enough such that there is at maximum one detection per time bin. Following the discrete time-evolution implemented by Eq. (6), the joint system-emission state at time T can be written as:

$$|\Psi(T)\rangle = \sum_{\{\sigma_n\}} K_{[M]}^{\sigma_M} \dots K_{[2]}^{\sigma_2} K_{[1]}^{\sigma_1} |\psi_S(0)\rangle \otimes |\sigma_1 \sigma_2 \dots \sigma_M\rangle, \quad (7)$$

where $\{\sigma_n\}$ denote all possible combinations of $\sigma_n = 0, 1$. In this expression we have used the Kraus operators

$$K_{[n]}^{\sigma_n} = \langle \sigma_n | U_{\text{SE}}^{[n]}(\Delta t) | 0_n \rangle, \quad (8)$$

which, to leading order in Δt , read:

$$\begin{aligned} K_0 &\equiv K_{[n]}^0 \approx 1 - i\omega S_x \Delta t - \frac{\Gamma}{2} S_+ S_- \Delta t, \\ K_1 &\equiv K_{[n]}^1 \approx \sqrt{\Delta t \Gamma} S_-, \end{aligned} \quad (9)$$

and thus do not depend on n . Note that quantum trajectories corresponding to ideal photocounting or homodyne detection can be obtained by performing the corresponding measurements on the time-bin modes appearing in the state in Eq. (7), see e.g. [19, 32].

B. Reduced state for time-bin modes

We are interested in the information that is contained in small portions of the output light field, as given by only few time-bin modes. When tracing out time-bin modes, the dynamics given by Eq. (6) can be conveniently implemented in terms of Kraus operators. Defining $\hat{\rho}(T) = |\Psi(T)\rangle\langle\Psi(T)|$, the corresponding reduced state of the system $\rho(T) = \text{Tr}_{\text{E}}\{\hat{\rho}(T)\}$ can also be obtained by successive applications of the CPTP map:

$$\rho(n\Delta t) = \mathcal{E}\rho([n-1]\Delta t), \quad \mathcal{E}\rho = K_0\rho K_0^\dagger + K_1\rho K_1^\dagger, \quad (10)$$

to the initial condition, which in the short time limit converges to the dynamics of Eq. (1). This approach allows us to efficiently study an intermediate situation in which instead of carrying on the full system-emission state $\hat{\rho}(T)$, we just keep track of the system and few time-bin modes. In the simplest case, we can trace out all time-bin modes but the n_1 -th one, obtaining the following state ($T = M\Delta t$):

$$\hat{\rho}_{[n_1]}(T) = \text{Tr}_{\text{E}\setminus[n_1]}\{\hat{\rho}(T)\}. \quad (11)$$

Similarly, we can define the reduced state of system and two time-bin modes:

$$\hat{\rho}_{[n_1, n_2]}(T) = \text{Tr}_{\text{E}\setminus[n_1, n_2]}\{\hat{\rho}(T)\}. \quad (12)$$

The dynamics of these joint states can be efficiently simulated by including the corresponding time-bin modes degrees of freedom (e.g. modes n_1 and n_2) in the system Hamiltonian (see Appendix A). In turn, if we are interested in the information contained only in the time-bin modes, we can further trace out the system obtaining the reduced states for one and two time-bin modes:

$$\begin{aligned} \hat{\mu}_{[n_1]}(T) &= \text{Tr}_{\text{S}}\{\hat{\rho}_{[n_1]}(T)\}, \\ \hat{\mu}_{[n_1, n_2]}(T) &= \text{Tr}_{\text{S}}\{\hat{\rho}_{[n_1, n_2]}(T)\}. \end{aligned} \quad (13)$$

In the short time limit, $N\Gamma\Delta t \ll 1$, we can use the short time expansion of the interaction unitary, i.e. Eq. (6), to obtain approximate expressions for the reduced states of the time-bin modes (see Appendix A). For the case of one time-bin mode that has interacted at time $t_1 = n_1\Delta t$ with the system, we obtain:

$$\begin{aligned} \hat{\mu}_{[n_1]} &\approx (1 - \Gamma\Delta t \langle S_+ S_- \rangle_{t_1}) |0_{n_1}\rangle\langle 0_{n_1}| \\ &\quad + \sqrt{\Gamma\Delta t} (\langle S_- \rangle_{t_1} |1_{n_1}\rangle\langle 0_{n_1}| + \text{H.c.}) \\ &\quad + \Gamma\Delta t \langle S_+ S_- \rangle_{t_1} |1_{n_1}\rangle\langle 1_{n_1}| + \mathcal{O}(\Delta t^{3/2}), \end{aligned} \quad (14)$$

where $\mathcal{O}(\Delta t^{3/2})$ denotes terms of order $\Delta t^{3/2}$. The notation $\langle \dots \rangle_t$ indicates that the expectation values are computed over the system reduced state at time t . In the case of two time-bin modes, the first interacting with the system at time t_1 and the second at time $t_2 = n_2\Delta t$, we obtain:

$$\begin{aligned} \hat{\mu}_{[n_1, n_2]} &\approx \hat{\mu}_{[n_1]} \otimes |0_{n_2}\rangle\langle 0_{n_2}| + |0_{n_1}\rangle\langle 0_{n_1}| \otimes \hat{\mu}_{[n_2]} \\ &\quad + \Gamma\Delta t \langle S_- \rangle_{t_1} |1_{n_1} 1_{n_2}\rangle\langle 0_{n_1} 0_{n_2}| \\ &\quad + \Gamma\Delta t \langle S_+ S_+ \rangle_{t_1} |0_{n_1} 0_{n_2}\rangle\langle 1_{n_1} 1_{n_2}| \\ &\quad + \Gamma\Delta t \langle S_+ \rangle_{t_1} |1_{n_1} 0_{n_2}\rangle\langle 0_{n_1} 1_{n_2}| \\ &\quad + \Gamma\Delta t \langle S_+ S_- \rangle_{t_1} |0_{n_1} 1_{n_2}\rangle\langle 1_{n_1} 0_{n_2}| \\ &\quad - |0_{n_1} 0_{n_2}\rangle\langle 0_{n_1} 0_{n_2}| + \mathcal{O}(\Delta t^{3/2}), \end{aligned} \quad (15)$$

where we have defined $\tau = (n_2 - n_1 - 1)\Delta t$, and we have used the definition of two-time correlations [87]:

$$\begin{aligned} \langle O_1(\tau) O_2 \rangle_{t_1} &= \text{Tr}\{O_1 e^{\mathcal{L}\tau} [O_2 \rho(t_1)]\}, \\ \langle O_1 O_2(\tau) \rangle_{t_1} &= \text{Tr}\{O_2 e^{\mathcal{L}\tau} [\rho(t_1) O_1]\}. \end{aligned} \quad (16)$$

In the short time limit, the reduced state of one time-bin mode contains information of the system at just a single time, while if we keep more time-bin modes we have access to system multi-time correlations [see Fig. 1]. In fact, in this limit, the reduced state of the system converges to the one described by the master equation (1) [86], while observables computed on one or two time-bin modes converge to quantities depending only on one- or two-time correlations of the system as computed with Eq. (1) (see Appendix A). Therefore, in this limit, the time-bin modes describe pieces of the output light field of the system modeled by the master equation (1) [86].

C. Very inefficient photodetection

We now discuss that the procedure of tracing out all time-bin modes except one or two occurs naturally when sampling very inefficiently the output light field, which corresponds to the use of inefficient photodetectors shown in Fig. 1. For finite system sizes, the Liouvillian \mathcal{L} is gapped, and its spectral gap defines the typical relaxation time of the system, $\tau_r = |\lambda_1|^{-1}$, where λ_1 is the eigenvalue with the smallest (in absolute value) nonzero real part. Correlations imprinted by the system on the output light field decay on this time scale, e.g. $\hat{\mu}_{[n_1, n_2]} \approx \hat{\mu}_{[n_1]} \otimes \hat{\mu}_{[n_2]}$ for $(n_2 - n_1 - 1)\Delta t \gg \tau_r$. Similarly, from the efficiency of our photodetectors, η , we can define the characteristic probing time $\tau_\eta = \Delta t/\eta$. From the point of view of the discrete-time output field, η can be seen as the probability to interrogate a time-bin mode. For $\eta = 1$ we have ideal continuous monitoring in which all time-bin modes participate in the measurement process and are thus interrogated. For $\eta \ll 1$ the sampling of the output field is poor and most of the time-bin modes are not interrogated, in which case the information contained in them is completely lost. More precisely, when $\tau_\eta \gg \tau_r$ the photocounting statistics is essentially Poissonian due to the dominating sampling inefficiency. In this regime of very inefficient photodetection, a single photodetector is mostly retrieving the information contained in $\hat{\mu}_{[n_1]}$. The use of an interferometer (Fig. 1) allows us to probe temporal correlations in this regime, as the measurement of a single time-bin mode at the output arms is ruled by $\hat{\mu}_{[n_1, n_2]}$, where $(n_2 - n_1 - 1)\Delta t$ is the time delay between the two paths (see Appendix B). In this limit, $\tau_\eta \gg \tau_r$, one is not able to follow the dynamics of the system by monitoring a photocount record. Dynamical effects are then only accessible by repeating the experiment many times in order to gather enough photons, or by studying the output of an interferometry setup during long observation times (Fig. 1).

IV. FUNDAMENTAL BOUNDS ON PARAMETER ESTIMATION

A. Parameter estimation with the emission field

Performing measurements on the system-emission joint state [Eq. (7)] we can implement a sensing protocol to estimate a parameter of interest. The precision at which a parameter can be estimated through any protocol is fundamentally bounded by the quantum Fisher information (QFI) of this joint state through the quantum Cramér-Rao bound [16, 27, 28]. We denote by $\Delta g(T)$ the variance on the estimated value of the parameter g over a measurement time window T . When the protocol makes use of an unbiased estimator, this can be expressed as:

$$\Delta g(T) \geq \frac{1}{\mathcal{F}_{\text{SE}}(g, T)} \quad (17)$$

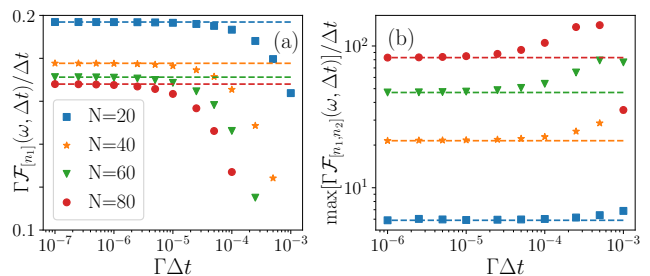


FIG. 3. **QFI in the short time limit.** (a) $\mathcal{F}_{[n_1]}(\omega, \Delta t)/\Delta t$ for the one time-bin reduced state (in the stationary state, $n_1 \gg 1$). (b) $\mathcal{F}_{[n_1, n_2]}(\omega, \Delta t)/\Delta t$ for the two time-bin reduced state optimized over the time difference between time bins. In both panels $\omega = 2\omega_c$. The dashed horizontal lines are a guide to the eye. The results of this figure indicate that for sufficiently small Δt the QFI scales linearly with the interaction time Δt .

where $\mathcal{F}_{\text{SE}}(g, T)$ is the QFI of the system-emission joint state at time T and parameter g . This quantity can be efficiently computed in the short time limit through a deformed master equation involving only the system degrees of freedom [16, 27, 30]. When the Liouvillian is gapped, the long-time behavior of this QFI is linear in T :

$$\lim_{T \rightarrow \infty} \frac{\mathcal{F}_{\text{SE}}(g, T)}{T} = \mathcal{F}_{\text{SE}}(g). \quad (18)$$

Moreover, for long-times the main contribution to this QFI comes from the information encoded in the output light field [32], as this grows with the measurement time T . In general, the system dynamics induces time-nonlocal correlations over the emission field, and thus one cannot generally retrieve the full sensitivity offered by the QFI with only time-local measurements, as e.g. photon counting [27]. A general recipe to perform the optimal measurement on the state (7) has been recently disclosed in Refs. [32, 33]. This involves cascading the output of the system to another system with the same degrees of freedom, and then performing time-local measurements on the joint output field. Recently, we have analyzed $\mathcal{F}_{\text{SE}}(\omega, T)$ and its optimal measurement protocol for the boundary time crystal [Eq. (1)] [72]. The most interesting results are displayed in the time-crystal phase in which the QFI displays the many-body enhanced scaling $\mathcal{F}_{\text{SE}}(\omega, T) \propto TN^2$. Moreover, a significant amount of this QFI can be retrieved by the cascaded protocol together with a simple photocounting strategy. The fundamental question we address in the following is whether this many-body scaling of the QFI is still present when considering only a small portion of the emitted field.

The reduced state of time-bin modes is generally a mixed state. For the one time-bin mode reduced state, the QFI is given by (see e.g. [2]):

$$\mathcal{F}_{[n_1]}(g, \Delta t) = 8 \lim_{\delta g \rightarrow 0} \frac{1 - \mathbb{F}(\hat{\mu}_{[n_1]}|_{g-\delta g}, \hat{\mu}_{[n_1]}|_{g+\delta g})}{(2\delta g)^2}, \quad (19)$$

where $\hat{\mu}_{[n_1]}|_{g\pm\delta g}$ denote the one time-bin mode state obtained evolving the full dynamics for the parameter values $g \pm \delta g$, respectively. This formula makes use of the Fidelity $\mathbb{F}(\hat{\mu}_1, \hat{\mu}_2) = \text{Tr}[\sqrt{\sqrt{\hat{\mu}_1}\hat{\mu}_2\sqrt{\hat{\mu}_1}}]$, which quantifies how sensitive is the state to a small parameter change. Similarly, in the two time-bin mode case, the QFI is given by:

$$\mathcal{F}_{[n_1, n_2]}(g, \Delta t) = 8 \lim_{\delta g \rightarrow 0} \frac{1 - \mathbb{F}(\hat{\mu}_{[n_1, n_2]}|_{g-\delta g}, \hat{\mu}_{[n_1, n_2]}|_{g+\delta g})}{(2\delta g)^2}, \quad (20)$$

where $\hat{\mu}_{[n_1, n_2]}|_{g\pm\delta g}$ correspond to the two time-bin modes reduced states obtained evolving the dynamics with parameter values $g \pm \delta g$.

In the short time limit, we find these QFI to display a linear scaling with Δt :

$$\begin{aligned} \lim_{\Delta t \rightarrow 0} \frac{\mathcal{F}_{[n_1]}(g, \Delta t)}{\Delta t} &= \mathcal{F}_{[n_1]}(g), \\ \lim_{\Delta t \rightarrow 0} \frac{\mathcal{F}_{[n_1, n_2]}(g, \Delta t)}{\Delta t} &= \mathcal{F}_{[n_1, n_2]}(g). \end{aligned} \quad (21)$$

We show this numerically in Fig. 3 for estimating the parameter ω , and considering n_1 large enough such that the system is in the stationary state ρ_{ss} . In Fig. 3 (a) we illustrate the one time-bin mode case, while in (b) the two time-bin mode case. In the latter, we show the QFI optimized over the time of the second bin, n_2 . Similarly to other quantities, we observe that the larger is N the smaller Δt needs to be in order to find convergence to the short time behavior. This reflects that the regime of validity for the expansion (6) is $N\Gamma\Delta t \ll 1$.

The quantum Cramér-Rao bound provides a link between the Fisher information and the lowest variance that can be achieved by performing measurements on these reduced states [2]. In particular, when measuring K times an observable \hat{A} on these reduced states, with $K \gg 1$, we obtain an estimation of a parameter g with the following variance:

$$\Delta g(K)|_{\hat{A}} = \frac{\Delta g|_{\hat{A}}}{K}, \quad (22)$$

where

$$\Delta g|_{\hat{A}} = (\langle \hat{A}^2 \rangle - \langle \hat{A} \rangle^2) \left| \frac{\partial \langle \hat{A} \rangle}{\partial g} \right|^{-2}, \quad (23)$$

and expected values $\langle \dots \rangle$ are taken with respect to $\hat{\mu}_{[n_1]}$ or $\hat{\mu}_{[n_1, n_2]}$. We refer to $\Delta g|_{\hat{A}}$ as the *estimation error*. The quantum Cramér-Rao bound reads as:

$$\Delta g(K)|_{\hat{A}} \geq \frac{1}{K\Delta t\mathcal{F}_q(g)}, \quad (24)$$

where $q = [n_1]$ or $q = [n_1, n_2]$, depending on whether the observable \hat{A} refers to one or two time-bin modes, respectively. Here, we have also assumed the short time limit in which a linear dependence of the QFI with Δt is found. From Eqs. (21) and (24) it becomes clear that we need

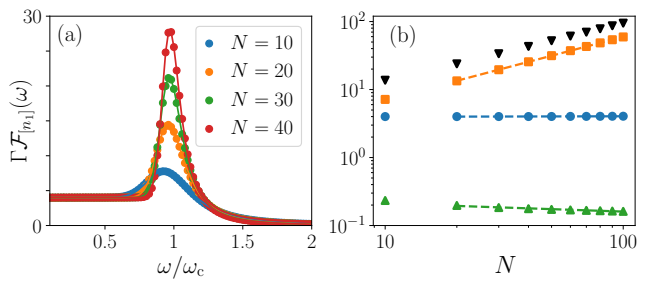


FIG. 4. **QFI per unit of time for one time-bin mode.** (a) $\mathcal{F}_{[n_1]}(\omega)$ varying ω/ω_c and N in the long-time limit, $n_1 \gg 1$. (b) Scaling of $\mathcal{F}_{[n_1]}(\omega)$ with N for $\omega/\omega_c = 0.5$ (blue circles), $\omega/\omega_c = 1$ (orange squares) and $\omega/\omega_c = 2$ (green triangles). The dashed lines correspond to a fit N^α of the largest N points, with exponents $\alpha = (0.01, 0.93, -0.12)$ for $\omega/\omega_c = (0.5, 1, 2)$, respectively. Black triangles correspond to $\mathcal{F}_{\text{SE}}(\omega)$ for $\omega/\omega_c = 1$ obtained in Ref. [72].

to measure many time-bin modes in order to achieve a significant precision in our sensing protocol, as the information acquired from a single time-bin is proportional to Δt . This can be understood as the sensing protocol becoming more precise as the effective measurement time $K\Delta t$ is increased.

In the following we focus on the estimation of the parameter ω , and we study $\mathcal{F}_{[n_1]}(\omega)$ and $\mathcal{F}_{[n_1, n_2]}(\omega)$ along the phase diagram, varying N . In turn, we compare $\mathcal{F}_{[n_1]}(\omega)$, $\mathcal{F}_{[n_1, n_2]}(\omega)/2$, and $\mathcal{F}_{\text{SE}}(\omega)$. This allows us to assess how probing the emission field in different ways affects the bound on sensitivity per unit of time. In this sense, $\mathcal{F}_{[n_1]}(\omega)$ bounds measurements that do not use any correlation in the field, $\mathcal{F}_{[n_1, n_2]}(\omega)$ bounds measurements that can exploit bipartite correlations present in the field, and $\mathcal{F}_{\text{SE}}(\omega)$ bounds measurements that can exploit any type of correlation.

B. QFI for single-time measurements of the emission field

We begin analyzing the case of a single time-bin mode reduced state for $n_1 \gg 1$, such that we probe the long-time statistics. In Fig. 4 (a) we show the QFI per unit of time in the short time limit, $\mathcal{F}_{[n_1]}(\omega)$, varying ω/ω_c and for different system sizes N . Well into the overdamped regime, $\omega/\omega_c < 1$, we observe the QFI to be constant and independent of N . In this case $\mathcal{F}_{[n_1]}(\omega)$ coincides with $\mathcal{F}_{\text{SE}}(\omega)$. This is because the system and emission field are in a product state, and the emission statistics is Poissonian [72]. The resulting value of the QFI per unit of time is $\mathcal{F}_{[n_1]}(\omega) \approx 4/\Gamma$ [72]. The QFI displays a peak at the phase transition, while it displays the smallest values in the time-crystal phase. In this sense, the QFI for probing the emission field at one time is qualitatively similar to the QFI of the stationary state of the system (see Ref. [40]).

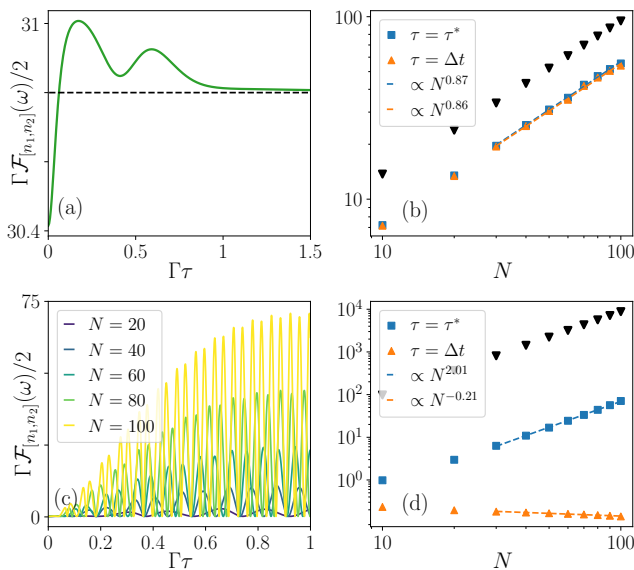


FIG. 5. **QFI per unit of time for the two time-bin modes state.** (a) Green solid line: $\mathcal{F}_{[n_1, n_2]}(\omega)/2$ for $\omega = \omega_c$, $N = 50$, and varying the time between the modes $\tau = (n_2 - n_1 - 1)\Delta t$. Black dashed line: $\mathcal{F}_{[n_1]}(\omega)$ for the same case. (b) $\mathcal{F}_{[n_1, n_2]}(\omega)/2$ for $\omega = \omega_c$ and varying N for two different cases: $n_2 = n_1 + 1$ (orange triangles), and for the optimal $\tau = \tau^*$ (blue squares) when the QFI is maximal. Black triangles correspond to $\mathcal{F}_{\text{SE}}(\omega)$ for the same parameter values [72]. Dashed lines correspond to a fit $\propto N^\alpha$ to the largest system sizes. (c) and (d) Same quantities but for the time-crystal phase $\omega = 2\omega_c$. In this case, in panel (c) various N are chosen.

At the phase transition point we observe the QFI to display a scaling $\propto N^{0.93}$ [see Fig. 4 (b)]. We also compare $\mathcal{F}_{[n_1]}(\omega)$ with $\mathcal{F}_{\text{SE}}(\omega)$. We observe that by just measuring one time-bin mode we get a significant amount of the total QFI per mode that we would get through measurements involving larger portions of the emission field. This might already be an advantage, since measurements involving only one time-bin mode may be simpler than protocols designed to exploit correlated portions of the emission field.

With regards to the oscillatory regime, Fig. 4 points out that measuring the emission field at just one time and when the system is in the stationary state is not useful. The advantage of the time-crystal phase comes from the dynamical correlations, which is not captured by just one time-bin mode in the long-time limit.

C. QFI for two-time measurements of the emission field

We now consider the QFI for the reduced two time-bin state in the short time limit and for $n_1 \gg 1$. In the two time-bin case, the interesting results are found when studying the QFI as a function of time [see Fig. 5]. We

omit from the analysis the overdamped regime, $\omega/\omega_c < 1$, since the time-bin modes are in a product state.

When considering two consecutive time-bin modes [i.e. $\tau = (n_2 - n_1 - 1)\Delta t = 0$] and for $n_1 \gg 1$, the QFI displays a similar pattern when varying ω/ω_c as that of the one time-bin mode case (not shown here). A peculiarity of the two consecutive time-bin mode case is that the QFI displays a slight subadditive behavior, i.e. $\mathcal{F}_{[n_1, n_1+1]}(\omega) < 2\mathcal{F}_{[n_1]}(\omega)$ [see Fig. 5 (a)]. Subadditive behavior has been reported for other systems [88], and it results from correlations acting in a detrimental way for parameter estimation. Nevertheless, the opposite behavior is also observed in our system at the critical point and in the oscillatory regime, where the QFI displays a maximum value for an optimal sensing time τ^* that depends on the parameter values, but not significantly on system size. This is shown in Fig. 5 for $\omega/\omega_c = 1$ and $\omega/\omega_c = 2$.

In Fig. 5 (a) we show the QFI per unit of time and varying τ (green solid line) for $\omega = \omega_c$ and $N = 50$. We also show the corresponding $\mathcal{F}_{[n_1]}(\omega)$ with a black dashed line. Subadditivity is observed for small τ , while for large τ we recover $\mathcal{F}_{[n_1, n_2]}(\omega) \rightarrow 2\mathcal{F}_{[n_1]}(\omega)$ when $n_2 \gg 1$, since the two time-bin modes become completely uncorrelated. A maximum for the QFI is found at time τ^* . In Fig. 5 (b) we compare this maximum QFI (blue squares) with the one for two consecutive time bins (orange triangles) varying N . We observe that, for $\omega = \omega_c$ they display almost the same scaling, and thus sensing at the optimal time only offers a small constant gain.

In Fig. 5 (c) and (d) we consider the same quantities in the time-crystal phase $\omega/\omega_c = 2$. In panel (c) we plot $\mathcal{F}_{[n_1, n_2]}(\omega)$ varying τ and N . Oscillations occur varying τ and displaying a frequency that is twice that of the magnetization dynamics, which is $\Omega = \sqrt{\omega^2 - \omega_c^2}$ [48]. While not visible in the plot, subadditive behavior is also observed for small τ , while for large τ the two time-bin mode reduced state factorizes. The QFI develops a maximum for $\Gamma\tau^* \sim 1$. The most interesting result comes when we analyze the behavior of the QFI varying N , see Fig. 5 (d). Here we find that at the optimal sensing time, the QFI displays the scaling $\mathcal{F}_{[n_1, n_2]}(\omega) \propto N^2$, recovering the same dependence with N as for the full system-emission joint state, $\mathcal{F}_{\text{SE}}(\omega)$ [72], and shown here in black triangles. While the scaling with N can be recovered considering just two time-bin modes, the QFI per unit of time of the system-emission joint state is still a factor 100 larger than that of the two time-bin modes per unit of time. This reveals that, higher order temporal correlations contain information that can substantially boost parameter estimation.

V. SENSITIVITY OF TWO-TIME MEASUREMENTS

In this section, we show that the QFI of two-time bin modes can be effectively exploited by correlated counting

measurements at two different times. In particular, we analyze measurement schemes that can be implemented with the Mach-Zehnder interferometer depicted in Fig. 1. We assume 50:50 beam splitters with a $\pi/2$ phase between reflection and a transmission. The input of arm '0' is the light emitted by the system through the collective channel, while the one of arm '1' is the vacuum. We then place one photon counter at each of the output arms '4' and '5'. The optical path difference is selected in order to match the time difference $\tau = (n_2 - n_1 - 1)\Delta t$ that we are interested in probing. We analyze the performance of photon counting measurements at each of the output arms, and also of the subtraction of both counting signals. This gives us access to the observables:

$$\hat{N}_{4(5)} = \hat{a}_{4(5)}^\dagger \hat{a}_{4(5)}, \quad \hat{N}_d = \hat{N}_5 - \hat{N}_4, \quad (25)$$

where $\hat{a}_{4,5}$ are the annihilation operators for the light field at the output arms. A detailed description of the interferometer in terms of time-bin modes is given in Appendix B, including the expression of $\hat{a}_{4,5}$ in terms of the input modes. The statistics of $\hat{N}_{4,5,d}$ can be fully characterized with the two time-bin modes reduced state $\hat{\mu}_{[n_1, n_2]}$. Their expected values with respect to this state read:

$$\begin{aligned} \langle \hat{N}_d \rangle &= \frac{1}{2} [\langle b_{[n_1]}^\dagger b_{[n_2]} \rangle e^{-i\Delta\phi} + \langle b_{[n_2]}^\dagger b_{[n_1]} \rangle e^{i\Delta\phi}], \\ \langle \hat{N}_{4,5} \rangle &= \frac{1}{4} [\langle b_{[n_1]}^\dagger b_{[n_1]} \rangle + \langle b_{[n_2]}^\dagger b_{[n_2]} \rangle \mp 2\langle \hat{N}_d \rangle], \end{aligned} \quad (26)$$

where the minus sign in the second equation corresponds to \hat{N}_4 , while the plus to \hat{N}_5 . Moreover, we have defined the phase difference $\Delta\phi = \omega_0\tau$. Varying the optical length of the two paths in Fig. 1 (b) results in an interference pattern for the number of counts. This pattern has two very distinct contributions: a very fast one due to $\Delta\phi$ with characteristic scale ω_0^{-1} , and a slow envelope of dynamical origin and with characteristic scale ω^{-1} . Because of our coarse-grained description, i.e. $\omega_0 \gg \omega$, we can decouple these two contributions and fix one value of $\Delta\phi$ to a good approximation, which we take $\Delta\phi = 0$ for convenience.

In the short time limit, we can use the approximate expression for the two time-bin modes reduced state [Eq. (15)] to calculate these expected values and the corresponding estimation errors. Probing the long-time dynamics ($n_1 \gg 1$), their leading contribution read:

$$\begin{aligned} \Delta\omega|_{\hat{N}_d} &\approx \frac{1}{\Gamma\Delta t} \frac{\langle S_+ S_- \rangle_{ss}}{|\partial_\omega \text{Re}[\langle S_+(\tau) S_- \rangle_{ss}]|^2}, \\ \Delta\omega|_{\hat{N}_{4,5}} &\approx \frac{2}{\Gamma\Delta t} \frac{\langle S_+ S_- \rangle_{ss} \mp \text{Re}[\langle S_+(\tau) S_- \rangle_{ss}]}{|\partial_\omega(\langle S_+ S_- \rangle_{ss} \mp \text{Re}[\langle S_+(\tau) S_- \rangle_{ss}])|^2}, \end{aligned} \quad (27)$$

We benchmark this expression with the exact dynamics in Fig. 6 (a), for the case of \hat{N}_d , while the cases of $\hat{N}_{4,5}$ are presented in Appendix B. As we can see, when $N\Gamma\Delta t$ becomes small enough, the color points (exact dynamics)

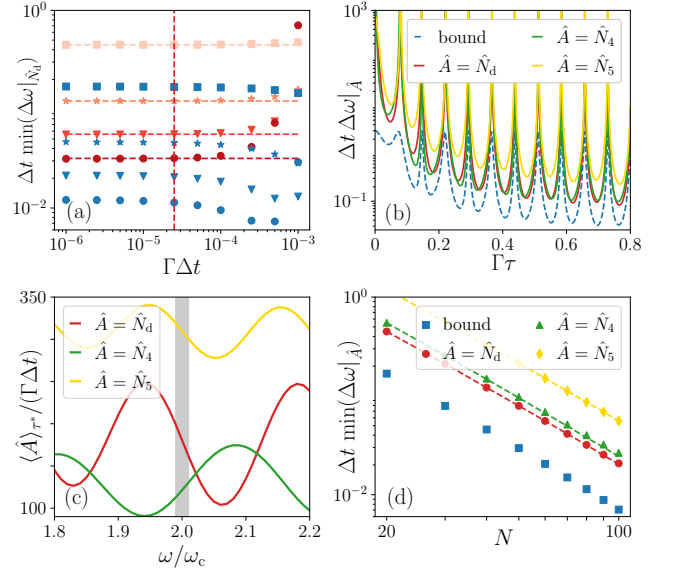


FIG. 6. Characterization of photon counting measurements after the interferometer. (a) Red symbols: estimation error $\Delta\omega|_{\hat{N}_d}$ at the optimal time τ^* varying $\Gamma\Delta t$ and N ($N = 20$ squares, $N = 40$ stars, $N = 60$ triangles, $N = 80$ circles). Dashed red lines correspond to the approximate results of Eq. (27), obtained calculating the two-time correlation functions with Eq. (1). Blue symbols correspond to the fundamental bound for the corresponding parameters. (b) Solid lines: $\Delta\omega|_{\hat{A}}$ as a function of the time between the time-bin modes τ and $N = 50$, for the three considered measurements, \hat{A} . Blue dashed line: fundamental bound on sensitivity given by the inverse of the two time-bin QFI per unit of time. (c) Expected values of the different counting measurements at their corresponding optimal time τ^* for sensing around $\omega/\omega_c = 2$ (shaded region). (d) Estimation error at the optimal sensing time τ^* for each of the three counting measurements and varying system size. The dashed lines correspond to the approximate results of Eq. (27). The chosen $\Gamma\Delta t = 2.5 \cdot 10^{-5}$ is indicated as a red-dashed vertical line in panels (a). The results of panels (a), (b) and (d) correspond to $\omega = 2\omega_c$.

converge to the dashed lines (approximate solution). In this case, we choose the value of the estimation error at the optimal sensing time τ^* at which the estimation error is minimized. We also compare it to the fundamental bound given by the QFI at the optimal sensing time (blue points), finding that this kind of measurement is close to optimal (roughly a factor 3 times the bound).

In Fig. 6 (b), we show that the estimation errors (solid lines) display a similar temporal pattern in τ as the inverse of the QFI (blue dashed line). Local minima are displayed separated by approximately half the mean-field period of oscillation. Both the bound and the estimation errors display an optimal sensing time τ^* at which they are minimized. Nevertheless, it is not crucial for the protocol to tune to this optimal time, but rather to select a τ close to one of the many minima, as they display similar estimation errors. While near the local minima

the bound and estimation errors display similar values, in between the minima the latter display values orders of magnitude larger. This variability results from a different susceptibility of $\langle S_+(\tau)S_- \rangle_{ss}$ to changes in ω within each period of the sinusoidal oscillations.

In Fig. 6 (c), we fix τ to the optimal time for $\omega/\omega_c = 2$ and each of the measurements, and we study how their expected values change with the Rabi frequency. This allows us to understand how the sensing protocols work around a particular value of ω/ω_c (shaded region). We observe that the optimal time corresponds (approximately) to the point of maximum derivative of the sinusoidal pattern. Notice that a value of $\langle \hat{N}_{d,4,5} \rangle$ is not generally associated to a unique Rabi frequency. As a consequence, these protocols can be used to sense small perturbations around a previously calibrated value of ω/ω_c .

In Fig. 6 (d), we analyze in more detail the behavior with N of the estimation error for the different measurements at their optimal sensing times. The color points correspond to the exact dynamics while the dashed lines to the results obtained from Eq. (27). They display similar scaling laws, in between $N^{-1.89}$ and $N^{-1.95}$, which are quite close to the one of the bound. While the protocol based on photon subtraction is the most sensitive, all of them display similar values. Therefore, we conclude that measurement protocols based on photon counting of the output of the interferometer provide a way to efficiently exploit the sensitivity of two-time measurements in the time-crystal phase.

From the results presented in Fig. 6 it becomes clear that the collective oscillations play a fundamental role in the sensitivity of the protocol. The presence of an optimal sensing time and the enhanced scaling with system size can be understood from the properties of $\langle S_+(\tau)S_- \rangle_{ss}$ and its derivative with ω . In fact, we can gain understanding from the following approximate expression for the derivative of two-time correlations with respect to ω (see Appendix C for more details):

$$\partial_\omega \langle S_+(\tau)S_- \rangle_{ss} \approx -\frac{I_{\text{inc}}\tau\partial_\omega\Omega}{2\Gamma} \sin \Omega\tau e^{-\Gamma_1\tau} \quad (28)$$

where $\Gamma_1 \approx \Gamma$ for $\omega/\omega_c = 2$, and the incoherent stationary intensity is defined as $I_{\text{inc}} = \Gamma(\langle S_+S_- \rangle_{ss} - \langle S_+ \rangle_{ss}\langle S_- \rangle_{ss})$. This formula has a maximum close to $\tau \sim \Gamma$, in accordance to our observations. Importantly, the only term proportional to N^2 is the incoherent intensity. Thus, the observed N^2 enhancement results from atom-atom correlations that build up in the oscillatory phase and which lead to $I_{\text{inc}} \propto N^2$ (see Ref. [48] for a characterization of these atom-atom correlations).

VI. LOCAL DECAY AS ADDITIONAL DECAY CHANNEL

Until now, we have considered the system to display just one collective decay channel. However, in practice, one might find more decay channels that remain typically

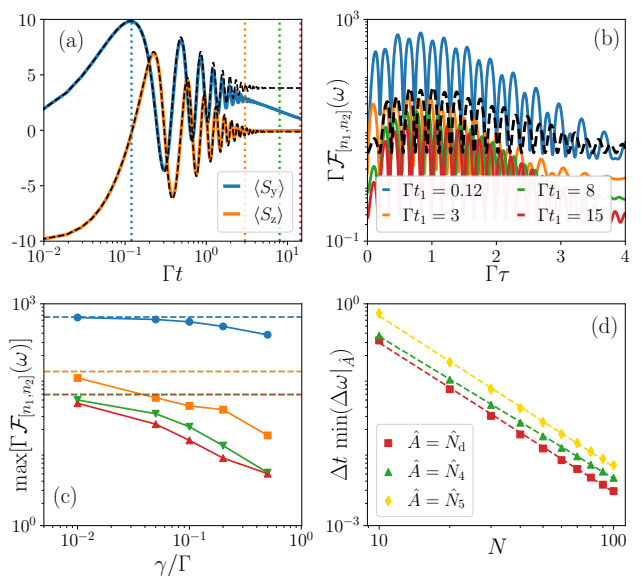


FIG. 7. **Impact of local decay.** (a) Dynamics of the collective magnetizations for $\omega/\omega_c = 2$, $N = 20$ $\gamma/\Gamma = 0.1$ and all atoms initially in the ground state. Black dashed lines correspond to the same case without local decay, $\gamma = 0$. (b) QFI per unit of time for the two time-bin mode reduced state varying τ and for the same parameters as in (a). Different lines correspond to different values of Γt_1 at which the first time-bin mode interacts with the system. Black dashed line corresponds to the two time-bin QFI in the stationary state without local decay. (c) Maximum QFI of the two time-bin reduced state varying γ/Γ for $\omega/\omega_c = 2$, $N = 20$ and the same Γt_1 's as in panel (b) (indicated by the same color code). Dashed lines display the QFI for $\gamma = 0$ and the corresponding Γt_1 . (d) Minimum estimation errors with respect to τ , and taking t_1 such that it coincides with the first maximum of $\langle S_y \rangle$ (blue lines and points in the other figures) varying N and for $\gamma/\Gamma = 0.1$. The results of this panel are obtained from Eq. (D1), derived in Appendix D. The dashed lines correspond to fits of the type $\propto N^{-\alpha}$ with $\alpha = (2.04, 1.92, 2.04)$ for \hat{N}_d , \hat{N}_4 and \hat{N}_5 , respectively. In all cases we take as initial condition all atoms in the ground state.

unmonitored. Here we address this general problem by considering the effects of local spontaneous emissions on the sensitivity of the time-crystal phase, and assuming that these channels are not monitored. Local decay is described by the following terms:

$$\mathcal{L}_{\text{loc}}\rho = \gamma \sum_{j=1}^N (\sigma_-^{(j)}\rho\sigma_+^{(j)} - \frac{1}{2}\{\sigma_+^{(j)}\sigma_-^{(j)}, \rho\}), \quad (29)$$

such that the master equation for the system reduced density matrix becomes $\partial_t\rho = (\mathcal{L} + \mathcal{L}_{\text{loc}})\rho$. The time-bin modes implementing the local decay channels give rise to a Kraus map that in the short time limit corresponds to $e^{\mathcal{L}_{\text{loc}}\Delta t}$ (as they remain unmonitored), which can be efficiently implemented exploiting the permutation symmetry of the system [89, 90].

For small local losses and the considered system sizes,

the collective dynamics manifests as a metastable transient response. This is illustrated in Fig. 7 (a) for $\omega/\omega_c = 2$, $N = 20$ and $\gamma/\Gamma = 0.1$. The dynamics in the presence of local decay is given by the colored solid lines, while black dashed lines correspond to the case without local decay and same initial state (all atoms in the ground state). We observe that both cases coincide until $\Gamma t \sim 3$, after which the effects of local decay dominate. In the following we focus on the system capability to perform parameter estimation during this metastable transient, rather than at stationarity, since our focus is on exploiting collective effects.

In Fig. 7 (b), we show the two time-bin mode QFI per unit of time varying τ and for different values of $t_1 = n_1 \Delta t$ with $N = 20$ and $\gamma/\Gamma = 0.1$. The considered values of t_1 are displayed as vertical dashed lines in panel (a). We observe that the QFI attains its largest values for the smallest Γt_1 . The dynamical behavior of the QFI for small $\Gamma \tau$ (until $\Gamma \tau \sim 3$) is similar to that in the absence of local losses (black dashed line). For larger $\Gamma \tau$ the oscillations and magnitude displayed by the QFI are attenuated due to the effects of local decay. In all cases the QFI displays an optimal sensing time τ^* at which it assumes the maximum value. In Fig 7 (c), we analyze how the maximum of the QFI varies with the local decay strength γ/Γ , and for different values of Γt_1 . For comparison we plot the respective maximum of the QFI for $\gamma = 0$ and the corresponding Γt_1 in color dashed lines. As we increase γ/Γ the maximum QFI diminishes. The effects of local decay are smaller for the smallest values of Γt_1 . This follows from the metastable character of the collective oscillations. Instead, for the largest Γt_1 and γ/Γ , the time-bin modes are essentially resolving the stationary state in the presence of local losses, which displays a smaller value of the QFI.

We now analyze the effects of local decay on the specific sensing protocols based on photon counting at the output of the interferometer (see Fig. 1). Within the metastable transient, the dynamics in τ of the estimation error are qualitatively similar to the case without local losses, also closely following the fundamental bound (not shown here). The approximate formulas of Eq. (27) work well also in the presence of local decay and in the short time limit (see Appendix D for more details). Notice that one has to evaluate the expectation values and two-time correlations in Eq. (27) using the total Liouvillian $\mathcal{L} + \mathcal{L}_{\text{loc}}$, and replacing the stationary time by the corresponding Γt_1 [see Eq. (D1)]. In Fig. 7 (d) we analyze the effects of increasing N on the estimation error at the optimal sensing time, $\Gamma \tau^* \sim 1$, and using Eq. (D1) that includes local decay and it is valid in the short time limit. We focus on the results obtained fixing Γt_1 to the first oscillation maximum of $\langle S_y \rangle$ ($\Gamma t_1 = 0.12$ in the case of $N = 20$). Similarly to the case without local decay, the measurement of \hat{N}_d is the one providing more sensitivity, although $\hat{N}_{4,5}$ display similar values. Remarkably, we observe an approximate quadratic scaling with particle number, N^{-2} , in all cases recovering the one observed

in the absence of local decay. We notice that this scaling is sensitive to the time Γt_1 , finding that at later times the scaling is no longer quadratic (see Appendix D). In this sense, in the presence of local losses, one could exploit the quadratic scaling in N using a pulsed scheme in which the system is periodically reset to the ground state in periods of the order of the optimal sensing time.

VII. DISCUSSION AND CONCLUSIONS

We have analyzed the problem of parameter estimation using the emitted light of a system displaying nonequilibrium collective phenomena. We have addressed the problem assuming very inefficient photodetection $\eta \ll 1$, thus facing a typical challenge found in experimental setups. In fact, the limit we consider here can be seen as the worst case scenario, since we are assuming that the poor detection efficiency does not allow us to probe temporal correlations induced by the collective phenomena, unless interferometric setups are used. In spite of these conditions, we have found collective enhancement of the sensitivity to parameter estimation. Our main results are a collective enhancement of the QFI bounding two-time measurements of the light field in the time-crystal phase, as well as the capacity to tap such sensitivity with photon detection at the output arms of a Mach-Zehnder interferometer (e.g. Fig. 1). More precisely, we have shown that the QFI of two-time bin modes displays a Heisenberg scaling N^2 when choosing the right time difference τ between the points at which the field is measured.

When comparing the QFI per unit of time of the two time-bin modes with the one of the full output field (obtained in [72]) we find that in the time-crystal phase the latter is a 100 times larger, even though they display the same scaling with N . Moreover, we recall that for a measurement time T , our very inefficient sampling reduces effectively the measurement time window to ηT . This reflects the intuitive result that a strategy that exploits the content of the full field is expected to be more sensitive. Nevertheless, the virtue of the approach presented here is that this is comparatively simpler and robust. In this sense, we expect that considering more ideal conditions, sensing protocols based on the output light of the time-crystal phase might display a sensitivity in between that of $\eta \ll 1$ and the one of the ideal limit $\eta = 1$, i.e., we expect the corresponding QFI per unit of time to lay in between the blue circles and the black triangles of Fig. 5 (d). Our analysis also provides a clear picture of which is the resource enhancing the sensitivity in the time-crystal phase, which might be useful when considering other situations. In particular, we have shown that efficient measurements probe the emission field around the maximum gradient point of the collective oscillations with respect to changes in the parameter ω [see Fig. 6], and that the N^2 sensitivity is rooted in the build up of atom-atom correlations in the oscillatory phase [see Eq. (28)].

Finally, we have addressed the general challenge of unobserved decay channels and how to tackle their detrimental effects. For the considered sizes, we have shown that for local losses up to the order of $\gamma/\Gamma \sim 0.1$ a metastable oscillatory transient persists, in which the estimation errors for counting measurements still display the N^{-2} enhancement. In this case, we propose the use of pulsed schemes in order to gather statistics about this interesting transient. We remark that the values of γ/Γ considered here are still comparatively small to those found in cavity QED setups in which collective atomic physics can be observed (see e.g. discussion in Ref. [44] or atom-cavity cooperativity values reported in, e.g., Refs. [82, 91]). However, in these scenarios, collective effects are enhanced by resorting on much larger atomic numbers such that the so-called strong collective coupling regime is reached. In this sense, our analysis highlights that the enhanced sensitivity manifests when the collective decay channel is the dominant one, and that we can overcome the presence of undesired decay channels by focusing on the collective effects present in the transient dynamics.

VIII. ACKNOWLEDGEMENTS

We thank F. Albarelli for interesting discussions. AC acknowledges support from the Deutsche Forschungsgemeinschaft (DFG, German Research Foundation) through the Walter Benjamin programme, Grant No. 519847240. FC is indebted to the Baden-Württemberg Stiftung for the financial support of this research project by the Eliteprogramme for Postdocs. We acknowledge the use of Qutip python library [92, 93]. We acknowledge funding from the Deutsche Forschungsgemeinschaft (DFG, German Research Foundation) through the Research Unit FOR 5413/1, Grant No. 465199066. We acknowledge support by the state of Baden-Württemberg through bwHPC and the German Research Foundation (DFG) through grant no INST 40/575-1 FUGG (JUSTUS 2 cluster). This work was supported by the QuantERA II programme (project CoQuaDis, DFG Grant No. 532763411) that has received funding from the EU H2020 research and innovation programme under GA No. 101017733.

Appendix A: Implementation of the discrete dynamics of the system plus one or two time-bin modes

System plus one time-bin mode. – We first assume that we are interested in keeping the state of the n_1 -th time-bin mode. After the interaction of the system with this time-bin mode, their joint reduced state is:

$$\hat{\rho}_{[n_1]}(n_1\Delta t) = e^{-iH_{[n_1]}\Delta t}(\mathcal{E}^{n_1-1}\rho(0)) \otimes |0_{n_1}\rangle\langle 0_{n_1}| e^{iH_{[n_1]}\Delta t}. \quad (\text{A1})$$

Here we have defined the Hamiltonian between the system and the n_1 -th time-bin:

$$H_{[n_1]} = \omega S_x + i\sqrt{\frac{\Gamma}{\Delta t}}[S_- b_{[n_1]}^\dagger - S_+ b_{[n_1]}], \quad (\text{A2})$$

whose action can be used to implement the input-output dynamics presented in Sec. III [86]. In order to further advance the dynamics keeping track of time-bin n_1 , we have to make use of the extended Hamiltonian:

$$H_{[n_1, n]} = \omega S_x + i\sqrt{\frac{\Gamma}{\Delta t}}[S_- \otimes \mathbb{I}_2 \otimes b_{[n]}^\dagger - S_+ \otimes \mathbb{I}_2 \otimes b_{[n]}]. \quad (\text{A3})$$

where \mathbb{I}_2 is the identity acting over the time-bin n_1 , while the label n denotes a subsequent time-bin mode. Notice that after Eq. (6) we have neglected two photon transitions, and thus we effectively treat the time-bin degrees of freedom as two-level systems. This amounts to the identification $b_{[n]} \rightarrow \hat{\sigma}_-$, $b_{[n]}^\dagger \rightarrow \hat{\sigma}_+$, where $\hat{\sigma}_\alpha$ ($\alpha = x, y, z, \pm$) are Pauli matrices. If we trace out the subsequent time-bin mode, the reduced state of system and time-bin n_1 evolves according to the map:

$$\hat{\rho}_{[n_1]}(n\Delta t) = \mathcal{E}_{[n_1]}\hat{\rho}_{[n_1]}((n-1)\Delta t) \quad (\text{A4})$$

defined as:

$$\mathcal{E}_{[n_1]}(\cdot) = K_{0, [n_1]}(\cdot)K_{0, [n_1]}^\dagger + K_{1, [n_1]}(\cdot)K_{1, [n_1]}^\dagger, \quad (\text{A5})$$

with

$$\begin{aligned} K_{0, [n_1]} &= \text{Tr}_{[n]} \{ e^{-iH_{[n_1, n]}\Delta t} (\mathbb{I}_S \otimes \mathbb{I}_2 \otimes |0_n\rangle\langle 0_n|) \}, \\ K_{1, [n_1]} &= \text{Tr}_{[n]} \{ e^{-iH_{[n_1, n]}\Delta t} (\mathbb{I}_S \otimes \mathbb{I}_2 \otimes |0_n\rangle\langle 1_n|) \}. \end{aligned} \quad (\text{A6})$$

where \mathbb{I}_S is the identity for the system. The reduced state for the n_1 -th time-bin, $\hat{\mu}_{[n_1]}(T)$, is then simply obtained by tracing out the system degrees of freedom.

System plus two time-bin modes. – We now want to obtain the joint reduced state of the system and two time-bin modes n_1 and n_2 , where $n_2 > n_1$. This reduced state just after the interaction with the second mode, i.e. $\hat{\rho}_{[n_1, n_2]}(n_2\Delta t)$, can be computed using the extended Hamiltonian (A3) and Kraus map (A4), which reads:

$$\begin{aligned} \hat{\rho}_{[n_1, n_2]}(n_2\Delta t) &= e^{-iH_{[n_2, n_1]}\Delta t} \hat{\rho}_{[n_1]}((n_2-1)\Delta t) \\ &\otimes |0_{n_2}\rangle\langle 0_{n_2}| e^{iH_{[n_2, n_1]}\Delta t}, \end{aligned} \quad (\text{A7})$$

where

$$\hat{\rho}_{[n_1]}((n_2-1)\Delta t) = \mathcal{E}_{[n_1]}^{n_2-n_1-1} \hat{\rho}_{[n_1]}(n_1\Delta t). \quad (\text{A8})$$

By tracing out the system, we can obtain the state $\hat{\mu}_{[n_1, n_2]}(n_2\Delta t)$. In order to further advance the dynamics of $\hat{\rho}_{[n_1, n_2]}(n_2\Delta t)$ we have to extend once more the discrete model to include additional degrees of freedom, similarly to what we have done in Eqs. (A3) and (A4). Nevertheless, this is only necessary if we want to keep more than two time-bin modes, as the information present in the reduced time-bin states, e.g. $\hat{\mu}_{[n_1, n_2]}(T)$, is actually

independent on what happens after the last interaction, i.e. it does not change for $T > n_2 \Delta t$. In this work, we focus on just one or two time-bin modes.

Short time limit. – In the short time limit $N\Gamma\Delta t \ll 1$, it can be useful to approximate the maps \mathcal{E} and $\mathcal{E}_{[n_1]}$ in terms of the action of master equations. This allows us to obtain the analytic approximate expressions for the time-bin modes reduced states presented in the main text, i.e. Eqs. (14) and (15). In particular, the map \mathcal{E} can be well approximated by $e^{\mathcal{L}\Delta t}$, where the Liouvillian is defined in Eq. (1). In turn, the extended map $\mathcal{E}_{[n_1]}$ can be well approximated by $e^{\mathcal{L}_{[n_1]}\Delta t} = e^{\mathcal{L}\Delta t} \otimes \mathbb{I}_2$, i.e.:

$$\begin{aligned} \mathcal{L}_{[n_1]}\hat{\rho}_{[n_1]} = & -i[\omega S_x \otimes \mathbb{I}_2, \hat{\rho}_{[n_1]}] + \Gamma(S_- \otimes \mathbb{I}_2 \hat{\rho}_{[n_1]} S_+ \otimes \mathbb{I}_2 \\ & - \frac{1}{2}\{S_+ S_- \otimes \mathbb{I}_2, \hat{\rho}_{[n_1]}\}), \end{aligned} \quad (\text{A9})$$

For finite system sizes N we have only one stationary state. The spectrum of \mathcal{L} is given by:

$$\mathcal{L}r_j = \lambda_j r_j, \quad l_j^\dagger \mathcal{L} = \lambda_j l_j^\dagger, \quad \text{Tr}_S\{l_j^\dagger r_k\} = \delta_{j,k}, \quad \rho_{ss} = r_0, \quad (\text{A10})$$

where the eigenvalues are ordered such that $\text{Re}[\lambda_j] \geq \text{Re}[\lambda_k]$ for $j > k$. Then, the spectrum of $\mathcal{L}_{[n_1]}$ is composed of the following tuples for each possible j that combine the eigenmatrices of \mathcal{L} with the basis elements of the time-bin Hilbert space:

$$\begin{aligned} \{l_{j,a}^\dagger\}_{a=0,1,2,3} &= \{l_j^\dagger \otimes \mathbb{I}_2, l_j^\dagger \otimes \hat{\sigma}_x, l_j^\dagger \otimes \hat{\sigma}_y, l_j^\dagger \otimes \hat{\sigma}_z\}, \\ \{r_{j,a}\}_{a=0,1,2,3} &= \{r_j \otimes \frac{\mathbb{I}_2}{2}, r_j \otimes \frac{\hat{\sigma}_x}{2}, r_j \otimes \frac{\hat{\sigma}_y}{2}, r_j \otimes \frac{\hat{\sigma}_z}{2}\}, \\ \{\lambda_{j,a}\}_{a=0,1,2,3} &= \{\lambda_j, \lambda_j, \lambda_j, \lambda_j\}. \end{aligned} \quad (\text{A11})$$

Thus the eigenvalues of $\mathcal{L}_{[n_1]}$ are those of \mathcal{L} four-fold degenerate. It follows that in the short time limit, the time evolution of the joint system-one-time-bin state can be written as:

$$\begin{aligned} \hat{\rho}_{[n_1]}(n\Delta t) = & \sum_{a=0}^3 \text{Tr}_{S,[n_1]}\{l_{0,a}^\dagger \hat{\rho}_{[n_1]}(n_1\Delta t)\} r_{0,a} \\ & + \sum_{j \geq 1} \sum_{a=0}^3 \text{Tr}_{S,[n_1]}\{l_{j,a}^\dagger \hat{\rho}_{[n_1]}(n_1\Delta t)\} r_{j,a} e^{\lambda_j(n-n_1)\Delta t}. \end{aligned} \quad (\text{A12})$$

Using that $\text{Tr}_S\{r_{j \geq 1, a}\} = 0$, we find that the reduced state of the time-bin only depends on the time $n_1 \Delta t$, and it is given by:

$$\hat{\mu}_{[n_1]} = \sum_{a=0}^3 \text{Tr}_{S,[n_1]}\{l_{0,a}^\dagger \hat{\rho}_{[n_1]}(n_1\Delta t)\} \text{Tr}_S\{r_{0,a}\}. \quad (\text{A13})$$

Similarly, in the stationary state of $\mathcal{L}_{[n_1]}$, correlations between system and time-bin have decayed out resulting in the following (initial condition dependent) stationary state:

$$\lim_{n \rightarrow \infty} \hat{\rho}_{[n_1]}(n\Delta t) = \rho_{ss} \otimes \hat{\mu}_{[n_1]}, \quad (\text{A14})$$

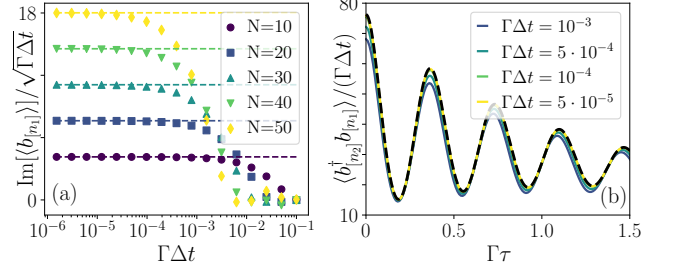


FIG. 8. Time-bin mode observables for short times. (a) Color points indicate the time-bin expectation value computed using the discrete time evolution varying $\Gamma\Delta t$ and for various N . Dashed lines correspond to the approximate result computed from Eqs. (14) with Eq. (1). The results are rescaled by $\sqrt{\Gamma\Delta t}$ and are computed for n_1 such that the system is in the stationary state. (b) Color points: two-time bin mode observables for $N = 20$, varying the time between time-bins $\Gamma\tau$ and for different values of $\Gamma\Delta t$. Dashed black line: result according to Eq. (15) computed with Eq. (1). The results have been scaled by $\Gamma\Delta t$. In both cases $\omega/\omega_c = 2$.

where $\hat{\mu}_{[n_1]}$ is given by Eq. (14). Moreover, from Eqs. (A11) and (A12) it also follows that the dynamics of any observable or multitime correlation that depends only on system degrees of freedom can be computed just using the system Liouvillian \mathcal{L} . This result is used in the derivation of Eq. (15), which contain system two-time correlations.

Numerical results in the short time limit. – In Fig. 8 we show that, as the short time limit is approached, observables depending on one-time bin and two-time bins approach the values corresponding to Eqs. (14) and (15). In particular, in Fig. 8 (a) we consider one time-bin mode observable for different system sizes N and varying the time Δt . The results obtained integrating the Kraus map (color points) approach those computed with Eq. (14) and the master equation as Δt diminishes. We notice that the larger the system size, the smaller needs to be the interaction time for both results to converge. This reflects the fact that the linear expansion in Eq. (6) is valid for $N\Gamma\Delta t \ll 1$. In Fig. 8 (b), we show an observable depending on two time-bin modes as a function of the time difference between the time-bin modes and for $N = 20$. We can see how as Δt diminishes the results computed with the Kraus map (color lines) converge to those predicted by Eq. (15) which depend on two-time correlations that are computed with the master equation. In both panels we have considered the dynamics in the oscillatory regime and for long times, $n_1 \gg 1$, such that the system has already reached its stationary state.

Appendix B: Mach-Zehnder interferometry of time-bin modes

Description of the interferometer. – In order to describe the Mach-Zehnder interferometer of Fig. 1 (b), we

adopt the Heisenberg picture for the light field operators. We consider 50 : 50 beam splitters with a $\pi/2$ phase difference between reflection and transmission. Then, the light field at the output of the first beam splitter is:

$$\begin{aligned}\hat{a}_2(t) &= \frac{1}{\sqrt{2}}[\hat{a}_0(t) + i\hat{a}_1(t)], \\ \hat{a}_3(t) &= \frac{1}{\sqrt{2}}[i\hat{a}_0(t) + \hat{a}_1(t)],\end{aligned}\quad (\text{B1})$$

where the subindex labels the different arms depicted in Fig. 1 (b). After this, the fields travel through the different arms acquiring a different phase and time delay. Then, the output of the second beam splitter is given by:

$$\begin{aligned}\hat{a}_4(t) &= \frac{1}{\sqrt{2}}[\hat{a}_2(t - \tau_2)e^{i\phi_2} + i\hat{a}_1(t - \tau_1)e^{i\phi_1}], \\ \hat{a}_5(t) &= \frac{1}{\sqrt{2}}[i\hat{a}_2(t - \tau_2)e^{i\phi_2} + \hat{a}_1(t - \tau_1)e^{i\phi_1}],\end{aligned}\quad (\text{B2})$$

where the time delays $\tau_{1,2}$ are given by the optical length of each arm, and the phases correspond $\phi_{1,2} = \omega_0\tau_{1,2}$. Notice that the relative phases pick up the carrier optical frequency ω_0 around which all our time scales are defined. Recall that an assumption of the input-output formalism is that $\omega_0 \gg \omega, \Gamma$, by orders of magnitude. This difference in orders of magnitude makes the rapidly oscillating interference pattern associated to these phases not relevant for our problem. This is because our results concern timescales of the order of ω^{-1} , which contain many cycles of ω_0 , hence allowing us to freely select a point of the interference pattern around the desired time separation $\tau = \tau_1 - \tau_2$. Nevertheless, for clarity, we keep accounting for these phases until the end of the derivation.

Relating the output fields to the input field, we obtain:

$$\begin{aligned}\hat{a}_4(t) &= \frac{1}{2}[\hat{a}_0(t - \tau_2)e^{i\phi_2} - \hat{a}_0(t - \tau_1)e^{i\phi_1}] \\ &\quad + \frac{i}{2}[\hat{a}_1(t - \tau_2)e^{i\phi_2} + \hat{a}_1(t - \tau_1)e^{i\phi_1}], \\ \hat{a}_5(t) &= \frac{i}{2}[\hat{a}_0(t - \tau_2)e^{i\phi_2} + \hat{a}_0(t - \tau_1)e^{i\phi_1}] \\ &\quad - \frac{1}{2}[\hat{a}_1(t - \tau_2)e^{i\phi_2} - \hat{a}_1(t - \tau_1)e^{i\phi_1}].\end{aligned}\quad (\text{B3})$$

We now assume that $\tau_2 < \tau_1$. We proceed with the discretization in time of the light field, making the correspondence $t - \tau_1 = n_1\Delta t$, $t - \tau_2 = n_2\Delta t$ with $n_2 > n_1$. The input of arm '0' contains the field emitted by the system, while the input of arm '1' is the vacuum. Then, we arrive to the following expression for the output of the Mach-Zehnder interferometer written in terms of time-bin modes:

$$\begin{aligned}\hat{a}_4(t) &= \frac{1}{2}[b_{[n_2]}e^{i\phi_2} - b_{[n_1]}e^{i\phi_1}] + \frac{i}{2}[c_{[n_2]}e^{i\phi_2} + c_{[n_1]}e^{i\phi_1}], \\ \hat{a}_5(t) &= \frac{i}{2}[b_{[n_2]}e^{i\phi_2} + b_{[n_1]}e^{i\phi_1}] - \frac{1}{2}[c_{[n_2]}e^{i\phi_2} - c_{[n_1]}e^{i\phi_1}],\end{aligned}\quad (\text{B4})$$

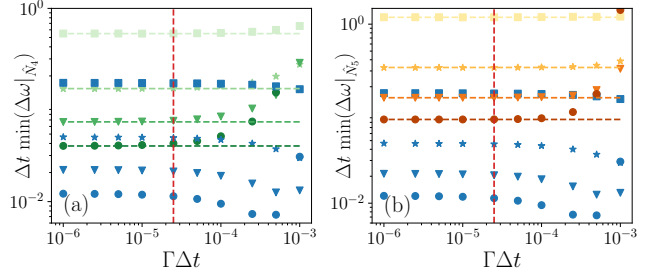


FIG. 9. **Counting measurements in the short time limit.** (a) Green symbols: estimation error $\Delta\omega|_{\hat{N}_4}$ at the optimal time τ^* varying $\Gamma\Delta t$ and N ($N = 20$ squares, $N = 40$ stars, $N = 60$ triangles, $N = 80$ circles). Dashed green lines correspond to the approximate results of Eq. (27), obtained using the master equation two-time correlation functions. Blue symbols correspond to the fundamental bound for the corresponding parameters. (b) Orange symbols: $\Delta\omega|_{\hat{N}_5}$ for the same cases as in (a). In both panels $\omega/\omega_c = 2$.

where $t = n\Delta t$, with $n > n_1, n_2$, and $c_{[n_1]}$ and $c_{[n_2]}$ are the annihilation operators for vacuum time-bin modes at times $n_1\Delta t$ and $n_2\Delta t$, respectively. Therefore, the interferometer is probing the following state:

$$\hat{\mu}_{[n_2, n_1]} \otimes |0_{c, n_2}\rangle\langle 0_{c, n_2}| \otimes |0_{c, n_1}\rangle\langle 0_{c, n_1}|. \quad (\text{B5})$$

As the vacuum modes 'c' are independent of the parameter we want to estimate, the QFI of this state is the same as that of $\hat{\mu}_{[n_2, n_1]}$. This is because the QFI of a product between states is the sum of QFIs of each state of the product [2], while the QFI for the vacuum state of modes 'c' is zero.

Photon counting at the output arms. – The photon counters depicted at the output arms of the interferometer, see Fig. 1 (b), give us access to the following observables:

$$\begin{aligned}\langle \hat{a}_4^\dagger \hat{a}_4 \rangle &= \frac{1}{4}[\langle b_{[n_1]}^\dagger b_{[n_1]} \rangle + \langle b_{[n_2]}^\dagger b_{[n_2]} \rangle \\ &\quad - \langle b_{[n_1]}^\dagger b_{[n_2]} \rangle e^{-i\Delta\phi} - \langle b_{[n_2]}^\dagger b_{[n_1]} \rangle e^{i\Delta\phi}], \\ \langle \hat{a}_5^\dagger \hat{a}_5 \rangle &= \frac{1}{4}[\langle b_{[n_1]}^\dagger b_{[n_1]} \rangle + \langle b_{[n_2]}^\dagger b_{[n_2]} \rangle \\ &\quad + \langle b_{[n_1]}^\dagger b_{[n_2]} \rangle e^{-i\Delta\phi} + \langle b_{[n_2]}^\dagger b_{[n_1]} \rangle e^{i\Delta\phi}],\end{aligned}\quad (\text{B6})$$

where expectation values $\langle \dots \rangle$ are taken with respect to the two time-bin mode reduced state, and we have dropped the irrelevant label t . Notice that the vacuum modes 'c' do not contribute to normal ordered observables. The subtraction of the signal of both counters gives us access to the following observable:

$$\hat{N}_d = \hat{a}_5^\dagger \hat{a}_5 - \hat{a}_4^\dagger \hat{a}_4, \quad (\text{B7})$$

whose expectation value has been presented in the main text. In order to compute the estimation error, we need to compute the following expectation values:

$$\begin{aligned}\langle (\hat{a}_4^\dagger \hat{a}_4)^2 \rangle &= \langle \hat{a}_4^\dagger \hat{a}_4^\dagger \hat{a}_4 \hat{a}_4 \rangle + \langle \hat{a}_4^\dagger \hat{a}_4 \rangle^2, \\ \langle (\hat{a}_5^\dagger \hat{a}_5)^2 \rangle &= \langle \hat{a}_5^\dagger \hat{a}_5^\dagger \hat{a}_5 \hat{a}_5 \rangle + \langle \hat{a}_5^\dagger \hat{a}_5 \rangle^2,\end{aligned}\quad (\text{B8})$$

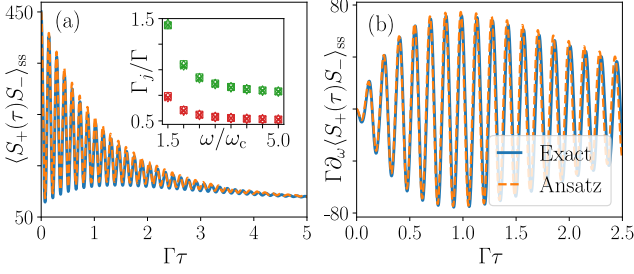


FIG. 10. **Ansatz for the two-time correlations in the oscillatory regime.** (a) Two time correlation $\langle S_+(\tau)S_- \rangle_{ss}$ computed using the exact dynamics (blue solid line) or the ansatz of Eq. (C2) (orange dashed line). (b) Derivative of the two time correlation using the exact dynamics (blue solid line) or Eq. (28) (orange dashed line). Parameters $N = 50$, $\omega/\omega_c = 2$. Inset: the two smallest (nonzero) decay rates of the Liouvillian, Γ_1 (red) and Γ_2 (green) for $N = 20$ (squares), $N = 50$ (diamonds) and $N = 100$ (crosses). The values are very similar for different system sizes.

which we have conveniently rewritten in normal order such that the vacuum modes 'c' do not contribute. Finally, in the short time limit, we can approximate the reduced two time-bin state by Eq. (15), which neglects two-photon transitions. From the dominant terms of Eq. (15), we observe that in this limit $\langle (\hat{a}_4^\dagger \hat{a}_4)^2 \rangle \approx \langle \hat{a}_4^\dagger \hat{a}_4 \rangle$ and $\langle (\hat{a}_5^\dagger \hat{a}_5)^2 \rangle \approx \langle \hat{a}_5^\dagger \hat{a}_5 \rangle$. This can be used to obtain the approximate formulas for the estimation error given in the main text. In Fig. 6, the approximated formula for the estimation error of associated with \hat{N}_d is benchmarked. In Fig. 9, we benchmark the expressions for the estimation errors of $\hat{N}_{4,5}$. Similarly to the case of \hat{N}_d , we observe that the results of numerically integrating the exact dynamics (color points) converge to the results given by Eq. (27) for $N\Gamma\Delta t \ll 1$.

Appendix C: Ansatz for the two-time correlations in the oscillatory regime

In this section we provide a simple ansatz for the two-time correlation $\langle S_+(\tau)S_- \rangle_{ss}$ in the oscillatory regime. We can write this two-time correlation in terms of the Liouvillian eigenmodes:

$$\langle S_+(\tau)S_- \rangle_{ss} = |\langle S_+ \rangle_{ss}|^2 + \sum_{j \geq 1} c_j e^{\lambda_j \tau}. \quad (\text{C1})$$

The coefficients c_j and eigenvalues λ_j can be obtained numerically. Our ansatz is based on keeping only the three first terms of the sum, i.e. those with the smallest decay rate, and propose a guess for their value. The eigenvalues are given by $\lambda_1 = -\Gamma_1$, $\lambda_{2,3} \approx \pm i\Omega - \Gamma_2$, where $\Omega = \sqrt{\omega^2 - \omega_c^2}$ is the frequency of the mean-field oscillatory solution. We numerically find $\Gamma_{1,2}$ not to vary significantly with system size and to display values of the order of Γ , see inset of Fig. 10 (a). The next step is to make a

guess for the coefficients $c_{1,2,3}$. Based on the fact that at $\tau = 0$ the two-time correlation takes the value $\langle S_+ S_- \rangle_{ss}$, we propose: $c_1 = I_{\text{inc}}/(2\Gamma)$, $c_2 = I_{\text{inc}}/(4\Gamma)$ and $c_3 = c_2^*$, with $I_{\text{inc}} = \Gamma(\langle S_+ S_- \rangle_{ss} - \langle S_+ \rangle_{ss} \langle S_- \rangle_{ss})$. We compute the involved stationary expectation values numerically, although one could use the analytical expressions of Ref. [48] which are already accurate for the considered sizes (not shown here). All together, our ansatz reads:

$$\langle S_+(\tau)S_- \rangle_{ss} \approx |\langle S_+ \rangle_{ss}|^2 + \frac{I_{\text{inc}}}{2\Gamma} (e^{-\Gamma_1 \tau} + \cos(\Omega\tau)e^{-\Gamma_2 \tau}). \quad (\text{C2})$$

We remark that with this ansatz we do not aim for perfect quantitative agreement but rather for an insightful formula that captures the main features of the collective response. This expression is benchmarked in Fig. 10 (a) for the case $N = 50$ and $\omega/\omega_c = 2$ finding good qualitative and quantitative agreement. We find a similar level of agreement when considering different system sizes (not shown here). We conclude that Eq. (C2) captures the main features of this correlation dynamics.

We now analyze the derivative with respect to ω of Eq. (C2). In principle, we should consider the derivative of all stationary expectation values as well as $\Gamma_{1,2}$. However, away from the phase transition, their contribution is small. In the spirit of keeping only the dominant terms we neglect these terms, obtaining:

$$\partial_\omega \langle S_+(\tau)S_- \rangle_{ss} \approx -\frac{I_{\text{inc}}\tau\partial_\omega\Omega}{2\Gamma} \sin(\Omega\tau)e^{-\Gamma_2\tau}, \quad (\text{C3})$$

which is the expression given in the main text. As we can observe in Fig. 10 (b), this approximate expression captures the main features of the exact dynamics, although it becomes less accurate for large τ . A similar level of agreement is found for different system sizes.

Appendix D: Additional results with local decay

Short time limit. – The approximate expression for the two time-bin mode reduced state given in Eq. (15) can also be used to analyze the short time limit in the presence of local dissipation. In such a case, one just needs to evaluate the expectation values and two-time correlations using the master equation with local decay, i.e. $\langle O \rangle_t = \text{Tr}\{Oe^{(\mathcal{L}+\mathcal{L}_{\text{loc}})t}\rho(0)\}$ and $\langle O_1(\tau)O_2 \rangle_{t_1} = \text{Tr}\{O_1e^{(\mathcal{L}+\mathcal{L}_{\text{loc}})\tau}[O_2\rho(t_1)]\}$. In Fig. 11 (a) we compare the two-time bin correlation $\langle b_{[n_2]}^\dagger b_{[n_1]} \rangle$ integrating the discrete-time dynamics (color lines) with the corresponding results obtained from adapting Eq. (15) to the presence of local losses (black-dashed lines). We show the case of $\omega/\omega_c = 2$, observing good agreement. Regarding the observed dynamics, we find that the smaller is Γt_1 the larger is the two time-bin correlation. Moreover, we observe that around $\Gamma\tau \sim 3$ there is a change in the behavior of $\langle b_{[n_2]}^\dagger b_{[n_1]} \rangle$, which comes from the effects of local decay on the dynamics.

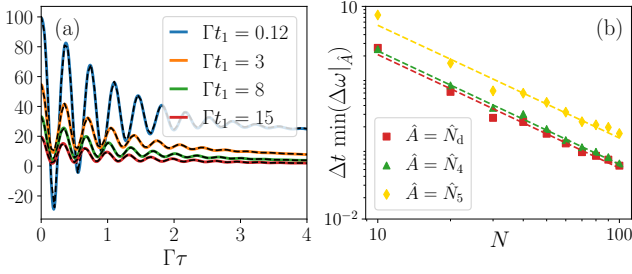


FIG. 11. **Additional results in the presence of local decay** (a) Two time-bin mode observables for short times and local decay for $\omega/\omega_c = 2$, $N = 20$, $\gamma/\Gamma = 0.1$, $\Gamma\Delta t = 10^{-4}$ and initial condition all atoms in the ground state. Color solid lines correspond to the results integrating the discrete time dynamics. Black dashed lines correspond to the approximate results obtained from Eq. (15) computing the expectation values and two-time correlations with the master equation including local decay. (b) Minimum estimation errors with respect to τ , and taking $\Gamma t_1 = 3$. The results of this panel are obtained from Eq. (D1). The dashed lines correspond to fits of the type $\propto N^{-\alpha}$ with $\alpha = (1.60, 1.60, 1.58)$ for \hat{N}_d , \hat{N}_4 and \hat{N}_5 , respectively. In all cases we take as initial condition all atoms in the ground state.

Estimation error formulas in the short time limit. – We can generalize the results of Eq. (27) to the case in which we have local decay and for finite $t_1 = n_1\Delta t$. In order to do so, we proceed as before, by computing the two time-bin reduced state of Eq. (15) with the master equation containing local losses. The expressions for the estimation errors of the counting observables are given by:

$$\Delta\omega|_{\hat{N}_d} \approx \frac{1}{2\Gamma\Delta t} \frac{\sum_{j=1,2} \langle S_+ S_- \rangle_{t_j}}{|\partial_\omega \text{Re}[\langle S_+(\tau) S_- \rangle_{t_1}]|^2},$$

$$\Delta\omega|_{\hat{N}_{4,5}} \approx \frac{2}{\Gamma\Delta t} \frac{\frac{1}{2} \sum_{j=1,2} \langle S_+ S_- \rangle_{t_j} \mp \text{Re}[\langle S_+(\tau) S_- \rangle_{t_1}]}{|\partial_\omega (\frac{1}{2} \sum_{j=1,2} \langle S_+ S_- \rangle_{t_j} \mp \text{Re}[\langle S_+(\tau) S_- \rangle_{t_1}])|^2}. \quad (\text{D1})$$

As discussed in the main text, the results are now sensitive to the choice of Γt_1 . In particular, in Fig. 11 (b) we show results for $\Gamma t_1 = 3$. We observe that the scaling N^{-2} is lost. Instead, one observes the approximate scaling law $N^{-1.6}$ which still surpasses the standard quantum limit. The results presented in Fig. 11 (b) display some non-monotonous behavior with N . This is because when fixing $\Gamma t_1 = 3$ and varying N , the point of the sinusoidal pattern of $\langle S_y \rangle_{t_1}$ that we are resolving varies with N .

-
- [1] C. L. Degen, F. Reinhard, and P. Cappellaro, Quantum sensing, *Rev. Mod. Phys.* **89**, 035002 (2017).
- [2] D. Braun, G. Adesso, F. Benatti, R. Floreanini, U. Marzolino, M. W. Mitchell, and S. Pirandola, Quantum-enhanced measurements without entanglement, *Rev. Mod. Phys.* **90**, 035006 (2018).
- [3] K. A. Gilmore, M. Affolter, R. J. Lewis-Swan, D. Barberena, E. Jordan, A. M. Rey, and J. J. Bollinger, Quantum-enhanced sensing of displacements and electric fields with two-dimensional trapped-ion crystals, *Science* **373**, 673 (2021).
- [4] A. Facon, E.-K. Dietsche, D. Grosso, S. Haroche, J.-M. Raimond, M. Brune, and S. Gleyzes, A sensitive electrometer based on a rydberg atom in a schrödinger-cat state, *Nature* **535**, 262 (2016).
- [5] M. Jing, Y. Hu, J. Ma, H. Zhang, L. Zhang, L. Xiao, and S. Jia, Atomic superheterodyne receiver based on microwave-dressed rydberg spectroscopy, *Nat. Phys.* **16**, 911 (2020).
- [6] V. Giovannetti, S. Lloyd, and L. Maccone, Quantum-enhanced measurements: beating the standard quantum limit, *Science* **306**, 1330 (2004).
- [7] D. J. Wineland, J. J. Bollinger, W. M. Itano, F. L. Moore, and D. J. Heinzen, Spin squeezing and reduced quantum noise in spectroscopy, *Phys. Rev. A* **46**, R6797 (1992).
- [8] M. Kitagawa and M. Ueda, Squeezed spin states, *Phys. Rev. A* **47**, 5138 (1993).
- [9] J. Ma, X. Wang, C.-P. Sun, and F. Nori, Quantum spin squeezing, *Physics Reports* **509**, 89 (2011).
- [10] D. Barberena, A. Chu, J. K. Thompson, and A. M. Rey, Trade-offs between unitary and measurement induced spin squeezing in cavity qed, *Phys. Rev. Res.* **6**, L032037 (2024).
- [11] I. D. Leroux, M. H. Schleier-Smith, and V. Vuletić, Implementation of cavity squeezing of a collective atomic spin, *Phys. Rev. Lett.* **104**, 073602 (2010).
- [12] O. Hosten, N. J. Engelsen, R. Krishnakumar, and M. A. Kasevich, Measurement noise 100 times lower than the quantum-projection limit using entangled atoms, *Nature* **529**, 505 (2016).
- [13] K. C. Cox, G. P. Greve, J. M. Weiner, and J. K. Thompson, Deterministic squeezed states with collective measurements and feedback, *Phys. Rev. Lett.* **116**, 093602 (2016).
- [14] B. Braverman, A. Kawasaki, E. Pedrozo-Peñafiel, S. Colombo, C. Shu, Z. Li, E. Mendez, M. Yamoah, L. Salvi, D. Akamatsu, Y. Xiao, and V. Vuletić, Near-unitary spin squeezing in ^{171}Yb , *Phys. Rev. Lett.* **122**, 223203 (2019).
- [15] H. M. Wiseman and G. J. Milburn, *Quantum measurement and control* (Cambridge university press, 2009).
- [16] C. Catana, M. van Horssen, and M. Guta, Asymptotic inference in system identification for the atom maser phil, *Trans. R. Soc. A* (2012).
- [17] S. Gammelmark and K. Mølmer, Bayesian parameter inference from continuously monitored quantum systems, *Phys. Rev. A* **87**, 032115 (2013).
- [18] L. Cortez, A. Chantasri, L. P. García-Pintos, J. Dressel, and A. N. Jordan, Rapid estimation of drifting parameters in continuously measured quantum systems, *Phys. Rev. A* **95**, 012314 (2017).
- [19] J. A. Gross, C. M. Caves, G. J. Milburn, and J. Combes,

- Qubit models of weak continuous measurements: Markovian conditional and open-system dynamics, *Quantum Sci. Technol.* **3**, 024005 (2018).
- [20] A. Shankar, G. P. Greve, B. Wu, J. K. Thompson, and M. Holland, Continuous real-time tracking of a quantum phase below the standard quantum limit, *Phys. Rev. Lett.* **122**, 233602 (2019).
- [21] M. A. C. Rossi, F. Albarelli, D. Tamascelli, and M. G. Genoni, Noisy quantum metrology enhanced by continuous nondemolition measurement, *Phys. Rev. Lett.* **125**, 200505 (2020).
- [22] G. Angelatos, S. A. Khan, and H. E. Türeci, Reservoir computing approach to quantum state measurement, *Phys. Rev. X* **11**, 041062 (2021).
- [23] A. Fallani, M. A. C. Rossi, D. Tamascelli, and M. G. Genoni, Learning feedback control strategies for quantum metrology, *PRX Quantum* **3**, 020310 (2022).
- [24] T. Ilias, D. Yang, S. F. Huelga, and M. B. Plenio, Criticality-enhanced quantum sensing via continuous measurement, *PRX Quantum* **3**, 010354 (2022).
- [25] E. Rinaldi, M. G. Lastre, S. G. Herrerros, S. Ahmed, M. Khanahmadi, F. Nori, and C. S. Munoz, Parameter estimation from quantum-jump data using neural networks, *Quantum Sci. Technol.* **9**, 035018 (2024).
- [26] T. Ilias, D. Yang, S. F. Huelga, and M. B. Plenio, Criticality-enhanced electric field gradient sensing with single trapped ions, *npj Quantum Inf.* **10**, 36 (2024).
- [27] S. Gammelmark and K. Mølmer, Fisher information and the quantum cramer-rao sensitivity limit of continuous measurements, *Phys. Rev. Lett.* **112**, 170401 (2014).
- [28] M. Guta and J. Kiukas, Equivalence classes and local asymptotic normality in system identification for quantum markov chains, *Commun. Math. Phys.* **335**, 1397 (2015).
- [29] C. Catana, L. Bouten, and M. Guță, Fisher informations and local asymptotic normality for continuous-time quantum markov processes, *J. Phys. A: Math. Theor.* **48**, 365301 (2015).
- [30] K. Macieszczak, M. Guță, I. Lesanovsky, and J. P. Garrahan, Dynamical phase transitions as a resource for quantum enhanced metrology, *Phys. Rev. A* **93**, 022103 (2016).
- [31] F. Albarelli, M. A. C. Rossi, M. G. A. Paris, and M. G. Genoni, Ultimate limits for quantum magnetometry via time-continuous measurements, *New J. Phys.* **19**, 123011 (2017).
- [32] D. Yang, S. F. Huelga, and M. B. Plenio, Efficient information retrieval for sensing via continuous measurement, *Phys. Rev. X* **13**, 031012 (2023).
- [33] A. Godley and M. Guta, Adaptive measurement filter: efficient strategy for optimal estimation of quantum Markov chains, *Quantum* **7**, 973 (2023).
- [34] E. M. Kessler, G. Giedke, A. Imamoglu, S. F. Yelin, M. D. Lukin, and J. I. Cirac, Dissipative phase transition in a central spin system, *Phys. Rev. A* **86**, 012116 (2012).
- [35] T. E. Lee, S. Gopalakrishnan, and M. D. Lukin, Unconventional magnetism via optical pumping of interacting spin systems, *Phys. Rev. Lett.* **110**, 257204 (2013).
- [36] F. Minganti, A. Biella, N. Bartolo, and C. Ciuti, Spectral theory of liouvillians for dissipative phase transitions, *Phys. Rev. A* **98**, 042118 (2018).
- [37] S. Fernández-Lorenzo and D. Porras, Quantum sensing close to a dissipative phase transition: Symmetry breaking and criticality as metrological resources, *Phys. Rev. A* **96**, 013817 (2017).
- [38] R. Di Candia, F. Minganti, K. Petrovnin, G. Paraoanu, and S. Felicetti, Critical parametric quantum sensing, *npj Quantum Inf.* **9**, 23 (2023).
- [39] V. P. Pavlov, D. Porras, and P. A. Ivanov, Quantum metrology with critical driven-dissipative collective spin system, *Phys. Scr.* **98**, 095103 (2023).
- [40] V. Montenegro, M. G. Genoni, A. Bayat, and M. G. Paris, Quantum metrology with boundary time crystals, *Commun. Phys.* **6**, 304 (2023).
- [41] U. Alushi, A. Coppo, V. Brosco, R. Di Candia, and S. Felicetti, Collective quantum enhancement in critical quantum sensing, *Commun. Phys.* **8**, 74 (2025).
- [42] D.-S. Ding, Z.-K. Liu, B.-S. Shi, G.-C. Guo, K. Mølmer, and C. S. Adams, Enhanced metrology at the critical point of a many-body rydberg atomic system, *Nat. Phys.* **18**, 1447 (2022).
- [43] M. Xu, D. A. Tieri, E. C. Fine, J. K. Thompson, and M. J. Holland, Synchronization of two ensembles of atoms, *Phys. Rev. Lett.* **113**, 154101 (2014).
- [44] M. Xu and M. J. Holland, Conditional ramsey spectroscopy with synchronized atoms, *Phys. Rev. Lett.* **114**, 103601 (2015).
- [45] A. Shankar, J. Cooper, J. G. Bohnet, J. J. Bollinger, and M. Holland, Steady-state spin synchronization through the collective motion of trapped ions, *Phys. Rev. A* **95**, 033423 (2017).
- [46] G. S. Agarwal, A. C. Brown, L. M. Narducci, and G. Vetri, Collective atomic effects in resonance fluorescence, *Phys. Rev. A* **15**, 1613 (1977).
- [47] P. Drummond and H. Carmichael, Volterra cycles and the cooperative fluorescence critical point, *Opt. Commun.* **27**, 160 (1978).
- [48] H. J. Carmichael, Analytical and numerical results for the steady state in cooperative resonance fluorescence, *J. Phys. B At. Mol. Opt.* **13**, 3551 (1980).
- [49] F. Iemini, A. Russomanno, J. Keeling, M. Schirò, M. Dalmonte, and R. Fazio, Boundary time crystals, *Phys. Rev. Lett.* **121**, 035301 (2018).
- [50] G. Ferioli, A. Glicenstein, I. Ferrier-Barbut, and A. Browaeys, A non-equilibrium superradiant phase transition in free space, *Nat. Phys.* , 1 (2023).
- [51] S. Agarwal, E. Chaparro, D. Barberena, A. P. n. Orioli, G. Ferioli, S. Pancaldi, I. Ferrier-Barbut, A. Browaeys, and A. Rey, Directional superradiance in a driven ultracold atomic gas in free space, *PRX Quantum* **5**, 040335 (2024).
- [52] D. Goncalves, L. Bombieri, G. Ferioli, S. Pancaldi, I. Ferrier-Barbut, A. Browaeys, E. Shahmoon, and D. E. Chang, Driven-dissipative phase separation in free-space atomic ensembles, arXiv preprint arXiv:2403.15237 (2024).
- [53] D. V. Else, C. Monroe, C. Nayak, and N. Y. Yao, Discrete time crystals, *Annu. Rev. Condens. Matter Phys.* **11**, 467 (2020).
- [54] Z. Gong, R. Hamazaki, and M. Ueda, Discrete time-crystalline order in cavity and circuit qed systems, *Phys. Rev. Lett.* **120**, 040404 (2018).
- [55] R. R. W. Wang, B. Xing, G. G. Carlo, and D. Poletti, Period doubling in period-one steady states, *Phys. Rev. E* **97**, 020202 (2018).
- [56] K. Tucker, B. Zhu, R. J. Lewis-Swan, J. Marino, F. Jimenez, J. G. Restrepo, and A. M. Rey, Shattered time: can a dissipative time crystal survive many-body

- correlations?, *New J. Phys.* **20**, 123003 (2018).
- [57] F. M. Gambetta, F. Carollo, M. Marcuzzi, J. P. Garrahan, and I. Lesanovsky, Discrete time crystals in the absence of manifest symmetries or disorder in open quantum systems, *Phys. Rev. Lett.* **122**, 015701 (2019).
- [58] B. Buča and D. Jaksch, Dissipation induced nonstationarity in a quantum gas, *Phys. Rev. Lett.* **123**, 260401 (2019).
- [59] B. Buča, J. Tindall, and D. Jaksch, Non-stationary coherent quantum many-body dynamics through dissipation, *Nat. Commun.* **10**, 1 (2019).
- [60] B. Zhu, J. Marino, N. Y. Yao, M. D. Lukin, and E. A. Demler, Dicke time crystals in driven-dissipative quantum many-body systems, *New J. Phys.* **21**, 073028 (2019).
- [61] H. Keßler, J. G. Cosme, M. Hemmerling, L. Mathey, and A. Hemmerich, Emergent limit cycles and time crystal dynamics in an atom-cavity system, *Phys. Rev. A* **99**, 053605 (2019).
- [62] A. Riera-Campeny, M. Moreno-Cardoner, and A. Sanpera, Time crystallinity in open quantum systems, *Quantum* **4**, 270 (2020).
- [63] A. Lazarides, S. Roy, F. Piazza, and R. Moessner, Time crystallinity in dissipative floquet systems, *Phys. Rev. Res.* **2**, 022002 (2020).
- [64] C. Lledó and M. H. Szymańska, A dissipative time crystal with or without z_2 symmetry breaking, *New J. Phys.* **22**, 075002 (2020).
- [65] K. Seibold, R. Rota, and V. Savona, Dissipative time crystal in an asymmetric nonlinear photonic dimer, *Phys. Rev. A* **101**, 033839 (2020).
- [66] G. Buonaiuto, F. Carollo, B. Olmos, and I. Lesanovsky, Dynamical phases and quantum correlations in an emitter-waveguide system with feedback, *Phys. Rev. Lett.* **127**, 133601 (2021).
- [67] M. Hajdušek, P. Solanki, R. Fazio, and S. Vinjanampathy, Seeding crystallization in time, *Phys. Rev. Lett.* **128**, 080603 (2022).
- [68] M. Krishna, P. Solanki, M. Hajdušek, and S. Vinjanampathy, Measurement-induced continuous time crystals, *Phys. Rev. Lett.* **130**, 150401 (2023).
- [69] A. Cabot, G. L. Giorgi, and R. Zambrini, Nonequilibrium transition between dissipative time crystals, *PRX Quantum* **5**, 030325 (2024).
- [70] H. Keßler, P. Kongkhambut, C. Georges, L. Mathey, J. G. Cosme, and A. Hemmerich, Observation of a dissipative time crystal, *Phys. Rev. Lett.* **127**, 043602 (2021).
- [71] B. Liu, L.-H. Zhang, Y. Ma, Q.-F. Wang, T.-Y. Han, J. Zhang, Z.-Y. Zhang, S.-Y. Shao, Q. Li, H.-C. Chen, *et al.*, Bifurcation of time crystals in driven and dissipative rydberg atomic gas, *Nat. Commun.* **16**, 1419 (2025).
- [72] A. Cabot, F. Carollo, and I. Lesanovsky, Continuous sensing and parameter estimation with the boundary time crystal, *Phys. Rev. Lett.* **132**, 050801 (2024).
- [73] F. Iemini, R. Fazio, and A. Sanpera, Floquet time crystals as quantum sensors of ac fields, *Phys. Rev. A* **109**, L050203 (2024).
- [74] D. Gribben, A. Sanpera, R. Fazio, J. Marino, and F. Iemini, Boundary time crystals as ac sensors: enhancements and constraints, arXiv preprint arXiv:2406.06273 (2024).
- [75] R. Demkowicz-Dobrzański, J. Kołodyński, and M. Guţă, The elusive heisenberg limit in quantum-enhanced metrology, *Nature communications* **3**, 1063 (2012).
- [76] P. Sekatski, M. Skotiniotis, J. Kołodyński, and W. Dür, Quantum metrology with full and fast quantum control, *Quantum* **1**, 27 (2017).
- [77] Y. L. Len, T. Gefen, A. Retzker, and J. Kołodyński, Quantum metrology with imperfect measurements, *Nature Communications* **13**, 6971 (2022).
- [78] T. B. Lantaño, D. Yang, K. Audenaert, S. Huelga, and M. Plenio, Unlocking heisenberg sensitivity with sequential weak measurement preparation, *Quantum* **9**, 1590 (2025).
- [79] V. Link, K. Luoma, and W. T. Strunz, Revealing the nature of nonequilibrium phase transitions with quantum trajectories, *Phys. Rev. A* **99**, 062120 (2019).
- [80] A. Cabot, L. S. Muhle, F. Carollo, and I. Lesanovsky, Quantum trajectories of dissipative time crystals, *Phys. Rev. A* **108**, L041303 (2023).
- [81] F. Carollo and I. Lesanovsky, Exact solution of a boundary time-crystal phase transition: Time-translation symmetry breaking and non-markovian dynamics of correlations, *Phys. Rev. A* **105**, L040202 (2022).
- [82] M. A. Norcia, M. N. Winchester, J. R. Cline, and J. K. Thompson, Superradiance on the millihertz linewidth strontium clock transition, *Sci. Adv.* **2**, e1601231 (2016).
- [83] J. A. Muniz, D. Barberena, R. J. Lewis-Swan, D. J. Young, J. R. Cline, A. M. Rey, and J. K. Thompson, Exploring dynamical phase transitions with cold atoms in an optical cavity, *Nature* **580**, 602 (2020).
- [84] C. Gardiner and P. Zoller, *Quantum noise: a handbook of Markovian and non-Markovian quantum stochastic methods with applications to quantum optics* (Springer Science & Business Media, 2004).
- [85] S. Arranz Regidor, G. Crowder, H. Carmichael, and S. Hughes, Modeling quantum light-matter interactions in waveguide qed with retardation, nonlinear interactions, and a time-delayed feedback: Matrix product states versus a space-discretized waveguide model, *Phys. Rev. Res.* **3**, 023030 (2021).
- [86] F. Ciccarello, S. Lorenzo, V. Giovannetti, and G. M. Palma, Quantum collision models: Open system dynamics from repeated interactions, *Phys. Rep.* **954**, 1 (2022).
- [87] H. Carmichael, *Statistical methods in quantum optics 1: master equations and Fokker-Planck equations*, Vol. 1 (Springer Science & Business Media, 1999).
- [88] M. Radaelli, G. T. Landi, K. Modi, and F. C. Binder, Fisher information of correlated stochastic processes, *New J. Phys.* **25**, 053037 (2023).
- [89] B. A. Chase and J. M. Geremia, Collective processes of an ensemble of spin-1/2 particles, *Phys. Rev. A* **78**, 052101 (2008).
- [90] B. Q. Baragiola, B. A. Chase, and J. Geremia, Collective uncertainty in partially polarized and partially decohered spin- $\frac{1}{2}$ systems, *Phys. Rev. A* **81**, 032104 (2010).
- [91] M. A. Norcia and J. K. Thompson, Strong coupling on a forbidden transition in strontium and nondestructive atom counting, *Phys. Rev. A* **93**, 023804 (2016).
- [92] J. Johansson, P. Nation, and F. Nori, Qutip: An open-source python framework for the dynamics of open quantum systems, *Comput. Phys. Commun.* **183**, 1760 (2012).
- [93] J. Johansson, P. Nation, and F. Nori, Qutip 2: A python framework for the dynamics of open quantum systems, *Comput. Phys. Commun.* **184**, 1234 (2013).